

Termination of the magnetorotational instability via parasitic instabilities in core-collapse supernovae

T. Rembiasz^{1,2}, M. Obergaulinger², P. Cerdá-Durán², E. Müller¹, M.A. Aloy²

¹ Max-Planck-Institut für Astrophysik, Karl-Schwarzschild-Str. 1, D-85748 Garching, Germany

² Departamento de Astronomía y Astrofísica, Universidad de Valencia, C/ Dr. Moliner 50, E-46100 Burjassot, Spain

Accepted 2015 December 9. Received 2015 December 9; in original 2015 July 31

ABSTRACT

The magnetorotational instability (MRI) can be a powerful mechanism amplifying the magnetic field in core collapse supernovae. Whether initially weak magnetic fields can be amplified by this instability to dynamically relevant strengths is still a matter of debate. One of the main uncertainties concerns the process that terminates the growth of the instability. Parasitic instabilities of both Kelvin-Helmholtz and tearing-mode type have been suggested to play a crucial role in this process, disrupting MRI channel flows and quenching magnetic field amplification. We perform two-dimensional and three-dimensional sheering-disc simulations of a differentially rotating proto-neutron star layer in non-ideal magnetohydrodynamics with unprecedented high numerical accuracy, finding that Kelvin-Helmholtz parasitic modes dominate tearing modes in the regime of large hydrodynamic and magnetic Reynolds numbers, as encountered close to the surface of proto-neutron stars. They also determine the maximum magnetic field stress achievable during the exponential growth of the MRI. Our results are consistent with the theory of parasitic instabilities based on a local stability analysis. To simulate the Kelvin-Helmholtz instabilities properly a very high numerical resolution is necessary. Using 9th order spatial reconstruction schemes, we find that at least 8 grid zones per MRI channel are necessary to simulate the growth phase of the MRI and reach an accuracy of $\sim 10\%$ in the growth rate, while more than ~ 60 zones per channel are required to achieve convergent results for the value of the magnetic stress at MRI termination.

Key words: accretion, accretion discs - MHD - instabilities - stars: magnetic field - supernovae: general

1 INTRODUCTION

Originally discovered by Velikhov (1959) and Chandrasekhar (1960), the magnetorotational instability (MRI) was suggested by Balbus & Hawley (1991, BH91 hereafter) to be the physical mechanism driving the redistribution of angular momentum required for the accretion process in Keplerian discs orbiting compact objects (see, e.g., Balbus & Hawley 1998, for a review).

Keplerian discs have a positive radial gradient in angular momentum, and therefore are linearly (Rayleigh-)stable. Purely hydrodynamic perturbations are unlikely to grow to amplitudes at which the associated stresses can account for efficient angular-momentum transport. In the presence of a weak magnetic field, however, a negative radial gradient in the angular velocity of the disc is MRI-unstable, and seed perturbations can grow exponentially on time scales close to the rotational period. During this phase, *channel modes* develop. Channel modes are pairs of coherent radial up- and downflows stacked vertically and threaded by layers of magnetic field of alternating radial and azimuthal polarity. In these modes, the magnetic tension (Maxwell stress tensor) transports angular

momentum along the field lines from the inner parts of the disc outwards.

The criterion for the MRI onset can be formulated in a rather simple manner, even if the thermal stratification (gradients of entropy or molecular weight) and non-ideal effects (viscosity, resistivity) are included (Balbus 1995; Menou et al. 2004). This allows for its application beyond Keplerian discs, in particular to proto-neutron stars (PNSs) resulting from the core-collapse of rotating massive stars. Simplified simulations by Akiyama et al. (2003) showed that such PNSs possess regions in which the MRI can grow on shorter time-scales than the time between the bounce and the successful explosion. This finding, later confirmed in multi-dimensional models (e.g. Obergaulinger et al. 2006b; Cerdá-Durán et al. 2007; Sawai et al. 2013; Sawai & Yamada 2015), presents the possibility of generating strong magnetic fields that can tap the rotational energy of the core, power magnetohydrodynamics (MHD) turbulence (Masada et al. 2015), and become a potentially important ingredient in rapidly-rotating core-collapse supernovae (CC-SNe).

How much these systems are affected by the MRI crucially depends on both its growth rate and on the final amplitude of the seed

perturbations. We can give an upper limit by assuming that the MRI ceases to grow once the magnetic field comes close (within a factor of α) to equipartition with the energy of the differential rotation. In CCSNe, this would correspond to dynamically important field strengths up to 10^{15} G. Similar energetic arguments can be used to express the MRI-generated stresses in the framework of α -disc models (Shakura & Sunyaev 1973).

This estimate neglects possible effects quenching the MRI before it reaches its maximally-allowed energy, and the effects of buoyancy as shown by Guilet & Müller (2015), who performed MRI simulations in the presence of buoyancy. They showed that the termination amplitude (at the end of the exponential growth) is not necessarily correlated to the magnetic field strength in the turbulent state that followed. The physics of the termination of the MRI growth remains an active field of research with many studies devoted to finding the value of the α parameter for the stress tensor. We refer, among others, to the works of Sano et al. (2004); Sano & Inutsuka (2001); Brandenburg (2005); Fromang & Papaloizou (2007); Gardiner & Stone (2005); Knobloch & Julien (2005).

The model of parasitic instabilities by Goodman & Xu (1994, GX94 hereafter), further studied and developed by Latter et al. (2009), Pessah & Goodman (2009) and Pessah (2010) provides a clear physical picture of the termination mechanism. The MRI channel modes are characterized by a shear layer and a current sheet in the vertical profiles of velocity and magnetic field, respectively. Hence, the (laminar) channel flows can be unstable against *secondary* (or *parasitic*) instabilities of Kelvin-Helmholtz (KH) or tearing-mode (TM) type.¹ Initially, the role of the parasites is negligible, as they grow much more slowly than the MRI. However, since the growth rate of the secondary instabilities is proportional to the channel mode amplitude, it is clear that at some stage the parasites will grow faster than the MRI channels whose growth rate is constant, whereas the parasites grow exponentially with time. Roughly at this point, the parasitic instabilities should disrupt the channel modes and terminate the MRI growth, marking the transition to the turbulent saturation phase (Pessah 2010). A further discussion of the MRI saturated state is beyond the scope of this paper.

Pessah (2010) analytically studied the MRI termination in resistive-viscous MHD by solving simplified model equations for the evolution of the parasitic instabilities. He identified different parameter-space regimes where, depending on hydrodynamic and magnetic Reynolds numbers, either the KH instability or the TM is the dominant (i.e. faster developing) secondary instability. Obergaullinger et al. (2014) found that the magnetic field at the surface of the PNS can be enhanced w.r.t. the interior regions. If this is also the case for rotating cores, MHD phenomena (like, e.g. the MRI) should be most prominent at the PNS surface. In this region, the Reynolds numbers are large if the surface is located above the neutrinosphere, which however may not always be the case (see Fig. 10 in Guilet et al. 2015). In this paper, we only investigate the regime of very high Reynolds numbers in which, according to the parasitic model, the MRI should be terminated by the KH instability.

The parasitic model has not been tested with direct global numerical simulations of the MRI in CCSNe. Obergaullinger et al. (2009) found in their semi-global 2D ideal MHD simulations that, because of numerical resistivity, the MRI was terminated by TMs. In their 3D simulations the MRI was terminated by non-

axisymmetric parasitic instabilities, although a clear identification of their nature was not possible.

To test the predictions of Pessah (2010), we performed a set of 2D and 3D resistive-viscous MHD simulations of the MRI. Given initial conditions, we studied in particular the importance of non-ideal effects by varying the values of both the uniform viscosity and uniform resistivity, which influence the growth of KH modes and of TMs, respectively. In the case of the KH instability, which is present already in ideal hydrodynamics, viscosity and resistivity alter the properties of the unstable modes merely quantitatively. On the other hand, TM are essentially driven by resistivity, i.e. they do not grow in ideal MHD, while viscosity plays a minor role by changing the properties of the unstable modes only quantitatively.

Since we are mainly concerned in this work with identifying the type of the parasitic instability that limits the growth of the MRI in particular models, we performed all our simulations (except for one control model) with a non-zero resistivity, but simulated models with both zero and non-zero viscosity. We defer a more thorough quantitative analysis of the influence of non-ideal effects to a subsequent work.

In Sec. 2 we give the criterion for the onset of the MRI, and we describe the initial stage of the instability during which channel modes develop. Next, we discuss possible scenarios of its termination, in particular, termination via the parasitic instabilities. In Sec. 3 we describe the numerical code and the initial setup used in our 2D and 3D simulations. We present the results of these simulations in Sec. 4, and summarize our findings in Sec. 5.

2 MRI EXPONENTIAL GROWTH PHASE AND TERMINATION

2.1 Physical model

We consider flows that can be described by the equations of resistive-viscous (non-ideal) MHD. In the presence of an external gravitational potential, Φ , these equations read

$$\partial_t \rho + \nabla \cdot (\rho \mathbf{v}) = 0, \quad (1)$$

$$\partial_t (\rho \mathbf{v}) + \nabla \cdot (\rho \mathbf{v} \otimes \mathbf{v} + \mathbf{T}) = -\rho \nabla \Phi, \quad (2)$$

$$\partial_t e_\star + \nabla \cdot \left[e_\star \mathbf{v} + \mathbf{v} \cdot \mathbf{T} + \eta \left(\mathbf{b} \cdot \nabla \mathbf{b} - \frac{1}{2} \nabla \mathbf{b}^2 \right) \right] = -\rho \mathbf{v} \cdot \nabla \Phi, \quad (3)$$

$$\partial_t \mathbf{b} + \nabla \cdot (\mathbf{v} \otimes \mathbf{b} - \mathbf{b} \otimes \mathbf{v}) = \eta \nabla^2 \mathbf{b}, \quad (4)$$

$$\nabla \cdot \mathbf{b} = 0, \quad (5)$$

where \mathbf{v} , ρ , η , and $\mathbf{b} \equiv \mathbf{B} / \sqrt{4\pi}$ are the fluid velocity, the density, a uniform resistivity, and the redefined magnetic field \mathbf{B} , respectively. The total energy density, e_\star , is composed of fluid and magnetic contributions, i.e. $e_\star = \varepsilon + \frac{1}{2} \rho \mathbf{v}^2 + \frac{1}{2} \mathbf{b}^2$ with the internal energy density ε and the gas pressure $p = p(\rho, \varepsilon, \dots)$. The stress tensor \mathbf{T} is given by

$$\mathbf{T} = \left[P + \frac{1}{2} \mathbf{b}^2 + \rho \left(\frac{2}{3} \nu - \xi \right) \nabla \cdot \mathbf{v} \right] \mathbf{I} - \mathbf{b} \otimes \mathbf{b} - \rho \nu \left[\nabla \mathbf{v} + (\nabla \mathbf{v})^T \right], \quad (6)$$

where \mathbf{I} is the unit tensor, and ν and ξ are the kinematic shear and bulk viscosity, respectively.

2.2 Magnetorotational instability

We study the MRI in a small portion of the rotating star at a given distance r from the rotation axis, embedded in a magnetic field. For convenience, we use cylindrical coordinates (r, ϕ, z) , hereafter. We restrict our analysis to locations close to the equatorial plane ($z = 0$) and vertical perturbation wavevectors for which the MRI is known

¹ Latter et al. (2009) classifies the types of parasitic modes differently.

to develop fastest (see, e.g. Balbus & Hawley 1998). In this case, we can consider a differentially rotating fluid with angular velocity Ω and linear velocity

$$\mathbf{v} = \Omega r \hat{\phi}, \quad (7)$$

threaded by a uniform vertical magnetic field

$$\mathbf{b} = b_{0z} \hat{\mathbf{z}} \quad (8)$$

in the local perturbation analysis. Here, $\hat{\phi}$ and $\hat{\mathbf{z}}$ are the unit vectors in ϕ and z direction, respectively.

With these assumptions and ignoring dissipative effects, the MRI instability criterion is (c.f. Balbus 1995)

$$N^2 + r \partial_r \Omega^2 = N^2 + \kappa^2 - 4\Omega^2 < 0, \quad (9)$$

where

$$\begin{aligned} N^2 &= \frac{\partial_r P}{\rho} \left(\frac{\partial_r \rho}{\rho} - \frac{\partial_r P}{\Gamma_1 P} \right), \\ \kappa^2 &= \frac{1}{r^3} \partial_r (r^4 \Omega^2), \end{aligned} \quad (10)$$

are the square of the Brunt-Väisälä frequency and the epicyclic frequency, respectively, and Γ_1 is the adiabatic index.

We consider an angular velocity with a radial dependence of the form

$$\Omega = \Omega_0 \left(\frac{r}{r_0} \right)^{-q}, \quad (11)$$

where Ω_0 is the angular velocity at the characteristic radius r_0 , and q is the local rotational shear given by

$$q = - \frac{d \ln \Omega}{d \ln r}. \quad (12)$$

The rotation profile (11) is quite generic for astrophysical systems, e.g. for $q = 3/2$, one recovers the Keplerian profile and for differentially rotating stars typical values of q are in the range $0 < q < 3/2$. The corresponding epicyclic frequency (i.e. the radial oscillation frequency) is

$$\kappa = \sqrt{2(2-q)}\Omega, \quad (13)$$

which vanishes at $q = 2$ (Rayleigh stability criterion limit for unmagnetised rotating fluids). We also assume that the entropy and composition are constant within the simulated volume, and hence $N^2 = 0$. The influence of entropy gradients on the MRI has been studied by Obergaulinger et al. (2009) and will not be discussed here.

If condition (9), is fulfilled, i.e. $0 < q < 2$, any perturbation of the form $e^{ik_z z + \gamma_{\text{MRI}} t}$ (WKB ansatz) is unstable for wavenumbers

$$k_z < k_{\text{crit}} = \sqrt{2q} \frac{\Omega}{c_{Az}}, \quad (14)$$

where $c_{Az} \equiv b_{0z} / \sqrt{\rho}$ is the Alfvén speed in the vertical direction.

BH91 considered small perturbations of the velocity, \mathbf{v}_c , and the magnetic field, \mathbf{b}_c , in a system whose velocity and magnetic field are given by Eqs. (7) and (8), respectively, i.e.

$$\mathbf{v} = \Omega r \hat{\phi} + \mathbf{v}_c, \quad (15)$$

$$\mathbf{b} = b_{0z} \hat{\mathbf{z}} + \mathbf{b}_c. \quad (16)$$

We note that one must also introduce appropriate perturbations of the other thermodynamical quantities to fulfil the MHD Eqs. (1) - (5), but we do not mention them here explicitly.

For the linearized ideal MHD equations in the incompressible

limit, BH91 found unstable solutions, which are usually referred to as *MRI channels*,

$$\mathbf{v}_c(t; k_{\text{MRI}}) = \tilde{v}_c e^{\gamma_{\text{MRI}} t} (\hat{\mathbf{r}} \cos \phi_v + \hat{\phi} \sin \phi_v) \sin(k_{\text{MRI}} z), \quad (17)$$

$$\mathbf{b}_c(t; k_{\text{MRI}}) = \tilde{b}_c e^{\gamma_{\text{MRI}} t} (\hat{\mathbf{r}} \cos \phi_b + \hat{\phi} \sin \phi_b) \cos(k_{\text{MRI}} z), \quad (18)$$

where the subscript c stands for *channel*, $\hat{\mathbf{r}}$ is the unit vector in r direction, \tilde{v}_c and \tilde{b}_c are the initial amplitudes, ϕ_v and ϕ_b are the angles between the r -axis and the direction of the velocity and magnetic field channels, respectively. The wavenumbers k_{MRI} correspond to values of k_z fulfilling Eq. (14). To simplify the notation, we define

$$v_c(t) = \tilde{v}_c e^{\gamma_{\text{MRI}} t}, \quad (19)$$

$$b_c(t) = \tilde{b}_c e^{\gamma_{\text{MRI}} t}, \quad (20)$$

and for brevity, we will often drop the explicit time dependence, i.e. $v_c = v_c(t)$ and $b_c = b_c(t)$. GX94 generalized the results of BH91, and they showed that the MRI channels are an exact solution of the ideal incompressible MHD equations in the *shearing sheet* (local) approximation. This approximation consists in transforming the equations to a frame corotating with a fiducial fluid element and linearising the rotational profile around a radius r_0 , i.e. $\Omega(r) \approx (r - r_0) \partial_r \Omega(r)|_{r_0}$. In this frame, the gravitational force and the centrifugal force balance each other for initially Keplerian accretion discs, but the Coriolis force has to be taken into account. In differentially rotating stars, additional pressure gradients are necessary to provide an equilibrium.

In the ideal MHD limit, the MRI growth rate and the channel angles, ϕ_v and ϕ_b , are given by

$$\gamma_{\text{MRI}} = \Omega \sqrt{\sqrt{(2-q)^2 + 8q \left(\frac{k_{\text{MRI}}}{k_{\text{crit}}} \right)^2} - (2-q) - 2q \left(\frac{k_{\text{MRI}}}{k_{\text{crit}}} \right)^2} \quad (21)$$

and

$$\phi_v = \arctan \left[\frac{c_{Az}^2 k_{\text{MRI}}^2 + \gamma_{\text{MRI}}^2}{2\gamma_{\text{MRI}} \Omega_0} \right], \quad (22)$$

$$\phi_b = \phi_v + \frac{\pi}{2}, \quad (23)$$

respectively. The amplitude ratio $\tilde{v}_c / \tilde{b}_c$ is a function of k_{MRI} and q (cf. Pessah & Chan 2008, PC08 hereafter). The mode with the wavenumber

$$k_{\text{MRI}} = \sqrt{1 - \frac{(2-q)^2}{4}} \frac{\Omega}{c_{Az}} \quad (24)$$

grows fastest at a rate

$$\gamma_{\text{MRI}} = \frac{q}{2} \Omega. \quad (25)$$

Note that we use capital letters in the subscripts to refer to the fastest-growing mode (γ_{MRI} and k_{MRI}) to distinguish it from generic unstable modes with growth rates $\gamma_{\text{MRI}} \leq \gamma_{\text{MRI}}$.

For the fastest-growing mode, the magnetic field and the velocity amplitudes are related by

$$v_c = \sqrt{\frac{q}{4-q}} c_{Ac}, \quad (26)$$

where $c_{Ac} \equiv b_c / \sqrt{\rho}$ is the Alfvén speed parallel to the MRI channel, and the channel angles are $\phi_v = \pi/4$ and $\phi_b = 3\pi/4$.

The properties of MRI modes change when viscosity or resistivity are present in the system. PC08 generalized the results of GX94 and showed that MRI channels (Eqs. (17) and (18)) are also exact solutions of the resistive-viscous incompressible MHD

equations in the shearing sheet approximation. They derived expressions for the growth rate γ_{mri} , the amplitude ratio v_c/b_c , and the channel angles ϕ_v and ϕ_b of MRI-unstable modes for arbitrary hydrodynamic and magnetic Reynolds numbers. Following PC08, we define these two (dimensionless) numbers as

$$R_e = \frac{c_{Az}^2}{\nu\Omega}, \quad (27)$$

$$R_m = \frac{c_{Az}^2}{\eta\Omega}. \quad (28)$$

We note that in the case of a zero entropy gradient the (most general) dispersion relation of Menou et al. (2004) reduces to the one analysed by PC08. Since we limit our studies to isentropic models, we can directly apply their results.

In resistive-viscous MHD, the channel angles, ϕ_v and ϕ_b , are given by

$$\phi_v = \arctan \left[\frac{c_{Az}^2 k_{\text{mri}}^2 + (\gamma_{\text{mri}} + k_{\text{mri}}^2 \eta)(\gamma_{\text{mri}} + k_{\text{mri}}^2 \nu)}{2\Omega_0(\gamma_{\text{mri}} + k_{\text{mri}}^2 \eta)} \right], \quad (29)$$

$$\phi_b = \arctan \left[\frac{-\Omega_0[2(\gamma_{\text{mri}} + k_{\text{mri}}^2 \eta) + q(\nu - \eta)k_{\text{mri}}^2]}{c_{Az}^2 k_{\text{mri}}^2 + (\gamma_{\text{mri}} + k_{\text{mri}}^2 \eta)(\gamma_{\text{mri}} + k_{\text{mri}}^2 \nu)} \right] \quad (30)$$

when transforming Eqs. (50) and (51) of PC08 into dimensional units. In general, velocity channels and magnetic channels are not orthogonal. However, it is evident that if $\nu = \eta$ (i.e. when the magnetic Prandtl number $P_m \equiv R_m/R_e = 1$), Eq. (30) reduces to Eq. (23), so that the shift of $\pi/2$ between ϕ_v and ϕ_b may also hold in the non ideal MHD limit.

As the expressions for the MRI growth rate γ_{mri} and the amplitude ratio v_c/b_c are quite complex, we do not give them here (the interested reader will find the details in PC08). Instead, we briefly discuss some of their key physical aspects.

Both resistivity and viscosity reduce the MRI growth rate. They also shift both the critical wavenumber k_{crit} and the most unstable wavenumber k_{MRI} to lower values than those given for ideal MHD by Eq. (14) and (24), respectively. This behaviour can be readily understood, as dissipative effects are more pronounced in the resistive-viscous regime (as they scale $\propto k_z^2$). The smaller the Reynolds numbers, the larger the growth rate reduction and the larger the shifts. Moreover, the magnetic Reynolds number has a bigger influence than the hydrodynamic one, because the nature of the MRI is more “magnetic” than “hydrodynamic”. For any Reynolds number, the MRI growth rate $\gamma_{\text{mri}}(k_z)$ tends to zero for sufficiently short wavevectors, i.e. $\gamma_{\text{mri}} \rightarrow 0$ for $k_z \rightarrow 0$ (see Eq. 21).

PC08 found analytic expressions for the growth rate γ_{MRI} , and the wavevector k_{MRI} of the fastest-growing mode only in some limiting cases, usually for very large or very small Reynolds numbers (e.g. for $R_m \gg 1$ and $R_e \ll 1$). We note that for $R_e, R_m \geq 10$ (which holds for core collapse supernovae outside the neutrinosphere) the ideal MHD expressions given in Eqs. (25) and (24) determine the values of the wavenumber and the growth rate of the fastest-growing mode with relative errors $\leq 10\%$ compared to the values obtained by the expressions of PC08.

The high conductivity of the degenerate matter in a supernova core implies very high magnetic Reynolds numbers. Using an order-of-magnitude estimate of $\eta \sim 10^{-4} \text{ cm}^2 \text{ s}^{-1}$ (Thompson & Duncan 1993), Eq. (28) yields

$$R_m = 10^{13} \left(\frac{b_{0z}}{10^{13} \text{ G}} \right)^2 \left(\frac{10^{14} \text{ g cm}^{-3}}{\rho} \right) \left(\frac{10^3 \text{ s}^{-1}}{\Omega} \right) \left(\frac{10^{-4} \text{ cm}^2 \text{ s}^{-1}}{\eta} \right). \quad (31)$$

Because the magnetic Reynolds number is so large, we can safely

neglect resistivity in the expressions for the growth rate and the wavelength of the MRI.

The molecular viscosity of supernova matter ($\nu \sim 0.4 \text{ cm}^2 \text{ s}^{-1}$) is only a few orders of magnitude larger than the resistivity, i.e. the respective hydrodynamic Reynolds number $R_e \sim 2.5 \times 10^9 \gg 1$ (Thompson & Duncan 1993). In the region below the neutrinosphere, however, the tight coupling between neutrinos and matter changes the situation. According to Guilet et al. (2015) the neutrino-matter interaction results in an effective viscosity that varies between a few $10^9 \text{ cm}^2 \text{ s}^{-1}$ deep inside the PNS and $10^{12} \text{ cm}^2 \text{ s}^{-1}$ near the neutrinosphere, i.e. one finds

$$R_e = 0.1 \left(\frac{b_{0z}}{10^{13} \text{ G}} \right)^2 \left(\frac{10^{14} \text{ g cm}^{-3}}{\rho} \right) \left(\frac{10^3 \text{ s}^{-1}}{\Omega} \right) \left(\frac{10^{10} \text{ cm}^2 \text{ s}^{-1}}{\nu_v} \right). \quad (32)$$

The above equation implies that the expressions for the growth rate and for the angles ϕ_b and ϕ_v (Eqs. 22-25), which are valid in the limit of ideal MHD, are not satisfied inside the PNS. Outside the neutrinosphere, the interaction between matter and neutrinos changes its character from diffusion to free streaming. In the free streaming regime neutrino drag damps fluctuations not like an effective viscosity, but like a drag force that is independent of the wavelength. Its impact on the MRI is therefore very different from the impact of a viscosity (Guilet et al. 2015). Neutrino drag is relevant not only outside but also significantly below the neutrinosphere as long as the dynamics of interest is happening at a wavelength shorter than the neutrino mean free path, which varies from a metre inside the PNS to several kilometre near its surface (see Fig. 5 in Guilet et al. 2015). Because of these complications we will not investigate this effect here and refer the reader to the studies of Masada et al. (2007, 2012) and Guilet et al. (2015).

2.3 MRI termination

2.3.1 Termination scenarios

MRI channels cannot grow indefinitely, because their energy would constantly increase, whereas the energy of the system contained in differential rotation, which provides the reservoir for the MRI, is finite. Hence, there must be a physical mechanism terminating MRI growth.

GX94 suggested that MRI channels being exact solutions of the MHD equations (in the shearing sheet and incompressible flow approximations) may be unstable against parasitic instabilities, which could terminate the MRI growth. They found in their analytic calculations (under the assumptions described in Sec. 2.3.2) that in ideal MHD (shear driven) KH modes can develop on top of MRI channels. GX94 also suggested that in resistive MHD, parasitic instabilities of the (current driven) TM type could develop, too. We note that the importance of magnetic reconnection for MRI termination was already discussed by BH91. Analytic calculations by Latter et al. (2009) in resistive MHD confirmed this hypothesis. Alternatively, if this scenario does not hold, the magnetic field of the MRI channels could grow to a dynamically relevant strength (when the Alfvén speed becomes comparable to the sound speed), violating the approximation of incompressibility. Consequently, the magnetic field pressure would become important and it could push matter towards magnetic null surfaces of the MRI channels, or MRI channels could become buoyancy unstable (GX94). Finally, small amplitude MRI channels emerging in an already (MRI-driven) turbulent state could be destroyed by non-linear mode-mode interactions or turbulent mixing (Latter et al. 2009).

In this paper, we only consider the first scenario, i.e. MRI ter-

mination via parasitic instabilities. In Sec. 2.3.2, we will briefly discuss assumptions and findings of the parasite model of Goodman & Xu (1994) and of its extension to resistive-viscous MHD by Pessah (2010).

2.3.2 Termination via parasitic instabilities

GX94 considered perturbations in a system with already well developed MRI channels (of the fastest-growing mode with k_{MRI}) given by

$$\mathbf{v} = -q\Omega_0(r - r_0)\hat{\phi} + \mathbf{v}_c(t; k_{\text{MRI}}) + \mathbf{v}_p(r, \phi, z, t), \quad (33)$$

$$\mathbf{b} = b_{0z}\hat{z} + \mathbf{b}_c(t; k_{\text{MRI}}) + \mathbf{b}_p(r, \phi, z, t), \quad (34)$$

where \mathbf{v}_p and \mathbf{b}_p are the velocity and the magnetic field of the parasitic instabilities, respectively.

Solving the equations governing the evolution of the secondary (parasitic) instabilities is a very challenging task, because MRI channels, which are treated as a background field for the perturbations, are non-stationary. Hence, standard techniques like an WKB ansatz cannot be used. To make this task more tractable for analytic studies, GX94 considered a stage of MRI growth when the amplitude of the MRI channels is much larger than the initial weak magnetic field, i.e. $b_c \gg b_{0z}$. The growth rate of the secondary instabilities γ_p (which scales $\propto b_c$) is then much larger than the MRI growth rate, i.e. $\gamma_p \gg \gamma_{\text{MRI}}$. Under these conditions the time evolution of the MRI channels, the Coriolis force (which is of the order of γ_{MRI}), the background shear flow, and the initial background magnetic field b_{0z} can be neglected. Hence, instead of searching for solutions to perturbations according to Eqs. (33) and (34), GX94 considered a more simplified system where the velocity and the magnetic field are given by

$$\mathbf{v}(t) = \mathbf{v}_c(t_0; k_{\text{MRI}}) + \mathbf{v}_p(r, \phi, z, t), \quad (35)$$

$$\mathbf{b}(t) = \mathbf{b}_c(t_0; k_{\text{MRI}}) + \mathbf{b}_p(r, \phi, z, t), \quad (36)$$

with $t_0 = \text{const.}$ being the time at which the secondary perturbations are imposed. Similar assumptions were also made by Latter et al. (2009) and Pessah (2010).

Pessah (2010) identified regions in parameter space, where depending on the values of the hydrodynamic and magnetic Reynolds numbers either KH or TM is the dominant (i.e. faster developing) secondary instability that terminates MRI growth. In particular, for the conditions prevailing in core collapse supernovae outside the PNS ($R_e, R_m \gg 1$) the exponential growth phase of the MRI should be terminated by KH instabilities. TM should be dominant only in very resistive media, i.e. if $R_m \lesssim 1$. Pessah (2010) also found that, in general, (shear driven) KH modes grow fastest along the MRI velocity channels, $\phi_{\text{KH}} = \phi_v$, whereas (current driven) TM grow fastest along the magnetic field channels, $\phi_{\text{TM}} = \phi_b$. One of the aims of this work is to test these predictions through numerical simulations.

3 METHOD

3.1 Code

We use the three-dimensional Eulerian MHD code AENUS (Obergaullinger 2008) to solve the MHD equations (1)–(5). The code is based on a flux-conservative, finite-volume formulation of the MHD equations and the constrained-transport scheme to maintain a divergence-free magnetic field (Evans & Hawley 1988). Using high-resolution shock-capturing methods (e.g. LeVeque 1992),

the code employs various optional high-order reconstruction algorithms including a total-variation-diminishing piecewise-linear (TVD-PL) reconstruction of second-order accuracy, a third-, fifth-, seventh- and ninth-order monotonicity-preserving (MP3, MP5, MP7 and MP9, respectively) scheme (Suresh & Huynh 1997), a fourth-order, weighted, essentially non-oscillatory (WENO4) scheme (Levy et al. 2002), and approximate Riemann solvers based on the multi-stage (MUSTA) method (Toro & Titarev 2006). We add terms including viscosity and resistivity to the flux terms in the Euler equations and to the electric field in the MHD induction equation. We treat these terms similarly to the fluxes and electric fields of ideal MHD, except for using an arithmetic average instead of an approximate Riemann solver to compute the interface fluxes. The explicit time integration can be done with Runge-Kutta schemes of first, second, third, and fourth order (RK1, RK2, RK3, and RK4), respectively.

Choosing appropriate numerical schemes for our 3D simulations is an important issue, because we want to keep the numerical viscosity and resistivity as low as possible without unnecessarily increasing the computational cost. Therefore, before applying the code to the MRI, we assessed its numerical viscosity and resistivity in an extended set of auxiliary simulations (Rembiasz et al., in preparation). We performed test calculations of linear-wave propagation and the TM instability, comparing the numerical solutions with (semi-) analytic solutions. Our tests show that the very low numerical dissipation of the MP9 scheme well justifies its larger stencil (requiring more ghost zones). In the TM simulations, the main contribution to the numerical dissipation comes from the spatial rather than the temporal discretisation errors. We do not observe any gain in accuracy when using the RK4 instead of the RK3 scheme. Because we expect these findings to hold also for MRI simulations, we performed the simulations reported here with the MP9 scheme, a MUSTA solver based on the HLLD Riemann solver, and an RK3 time integrator (Harten 1983; Miyoshi & Kusano 2005).

3.2 Equation of state

We use the hybrid equation of state (EOS) of Keil et al. (1996), in which the gas pressure P results from the addition of two contributions, namely a baryonic one P_b and a thermal one P_{th} . These pressure contributions are given by

$$P_b = K\rho^{\Gamma_b}, \quad (37)$$

$$P_{\text{th}} = (\Gamma_{\text{th}} - 1)e_{\text{th}}, \quad (38)$$

where $K = 4.897 \times 10^{14}$ is the polytropic constant, and $\Gamma_b = 1.31$ and $\Gamma_{\text{th}} = 1.5$ are the barotropic index and the thermal adiabatic index, respectively. The quantity e_{th} is the thermal part of the internal energy e , i.e. $e_{\text{th}} = e - P_b/(\Gamma_b - 1)$.

3.3 Computational grid and boundary conditions

Our study comprises a set of two-dimensional axisymmetric simulations and a set of three-dimensional simulations. For both kinds of simulations we employed cylindrical coordinates (r, ϕ, z) and a computational domain centred around the equatorial plane at a radius $r_0 = 15.5 \text{ km}$. For this value of r_0 our computational box is located in the middle of a nascent PNS of radius $r_{\text{PNS}} \approx 30 \text{ km}$. However, Guilet et al. (2015) have recently shown that the viscosity due to neutrinos can be much higher in collapsing cores than previously thought. Close to the neutrinosphere, i.e. whenever the

neutrino mean free path is shorter than the length scale of interest, very low Reynolds numbers are expected. The most favorable place for MRI amplification is located close to the PNS star surface, where differential rotation is stronger, and the Reynolds numbers are larger if the surface is located above the neutrinosphere, which however may not always be the case (see Fig. 10 in Guilet et al. 2015). However this recent finding does not invalidate our studies as our models can be easily scaled for different initial conditions. We may choose different values of the radius, r , rotational velocity, Ω , or density, ρ , and scale the key physical quantities in following way:

$$\mathcal{M}_{r\phi} = \bar{\mathcal{M}}_{r\phi} \left(\frac{r}{r_0} \right)^2 \left(\frac{\Omega}{\Omega_0} \right)^2 \left(\frac{\rho}{\rho_0} \right), \quad (39)$$

$$b = \bar{b} \left(\frac{r}{r_0} \right) \left(\frac{\Omega}{\Omega_0} \right) \left(\frac{\rho}{\rho_0} \right)^{1/2}, \quad (40)$$

$$t = \bar{t} \left(\frac{\Omega}{\Omega_0} \right)^{-1}, \quad (41)$$

$$\gamma_{\text{MRI}} = \bar{\gamma}_{\text{MRI}} \left(\frac{\Omega}{\Omega_0} \right), \quad (42)$$

$$\lambda_{\text{MRI}} = \bar{\lambda}_{\text{MRI}} \left(\frac{r}{r_0} \right), \quad (43)$$

$$L_i = \bar{L}_i \left(\frac{r}{r_0} \right), \quad (44)$$

where $\Omega_0 = 1824 \text{ s}^{-1}$, and $\rho_0 = 2.47 \times 10^{13} \text{ g cm}^{-3}$, L_i is the box length in the direction i (where $i = r, \phi, z$), and the barred quantities are the values set up in or computed from our simulations. We stress again that the most favorable place for the development of the MRI is the region close to the surface of the PNS, where the differential rotation gradient and the Reynolds numbers are larger than deep inside the PNS. Since the choice of Ω_0 is ad hoc, it is evident that the ratio Ω/Ω_0 can be made as close as desired to one. This means that neither the MRI growth rate nor the typical growth time will change under a translation of the box to the surface of the PNS. Such a translation will also imply that $r/r_0 \sim 2$, while $\rho/\rho_0 \sim 0.1$, hence, the typical magnetic fields and Maxwell stresses would be 0.6 and 0.4 times smaller than in our models. However, as we will show, none of these variations would change the foremost qualitative prediction of our models, namely, that the termination of the MRI growth in collapsing stellar cores happens by the action of parasitic KH modes.

In the 3D simulations, the typical box size is $L_r \times L_\phi \times L_z = 1 \text{ km} \times 4 \text{ km} \times 1 \text{ km}$ in r, ϕ , and z direction, while the typical box size is $1 \text{ km} \times 1 \text{ km}$ in the (r, z) plane in our 2D simulations. We performed simulations involving up to $200 \times 800 \times 200$ zones (see Table 1).

We assume periodic boundary conditions in both ϕ and z -direction. This choice is natural for the ϕ direction, whereas in the vertical direction, z , the core is obviously not periodic. However, for the simulated region near the equatorial plane the vertical component of the gravitational force, F_{gz} , can be neglected, because it is much smaller than the radial one, i.e. $F_{gz}/F_{gr} \lesssim 0.03$.

Unlike in local simulations of accretion discs, we cannot use the shearing sheet boundary condition (see Hawley & Balbus 1991) in the radial direction, because it does not allow for global gradients of thermodynamic variables (which are present in core collapse supernovae) in the simulation domain. Therefore, like Obergaulinger et al. (2009) (who followed Klahr & Bodenheimer 2003), we use the shearing disc boundary condition, which allows one to take these gradients into account.

We solve the full compressible MHD equations and do not perform a transformation to the frame corotating with the fluid, which discriminates our simulations from the common shearing-box approach. In radial direction, we apply periodic boundary conditions to the deviation of a variable (here, density) from its initial background state, e.g.

$$\delta\rho(r, t) \equiv \rho(r, t) - \rho(r, 0), \quad (45)$$

i.e. we enforce periodicity of the perturbations. We apply these boundary conditions to angular velocity, density, momentum, and entropy. Because the initial magnetic field is homogeneous in all our simulations, we use periodic boundary conditions for this quantity too.

3.4 Initial conditions

Like Obergaulinger et al. (2009), we use equilibrium initial models based on the final stages of post-bounce cores from Obergaulinger et al. (2006a), in which (several tens of milliseconds after core bounce) the shock wave has reached distances of a few hundred kilometres and the post-shock region exhibits a series of damped oscillations as the PNS relaxes into a *nearly* hydrostatic configuration.

The rotational profile (given by Eq. 11 with $q = 1.25$) that we used in our simulations, is similar to the one employed in the global MRI simulations of Obergaulinger et al. (2006a). Because the resulting centrifugal force is insufficient to balance gravity, the gas is kept in (an initial hydrostatic) equilibrium by an additional pressure gradient, so that

$$\rho\partial_r\Phi - \partial_rP + r\rho\Omega^2 = 0. \quad (46)$$

The initial distributions of angular velocity, density, and gravitational potential are depicted in Fig. 1.

Unless otherwise stated, we set the initial magnetic field strength to $b_{0z} = 4.6 \times 10^{13} \text{ G}$, the shear and bulk viscosity to $\nu = \xi = 0 \text{ cm}^2 \text{ s}^{-1}$, and the resistivity to $\eta = 4.45 \times 10^8 \text{ cm}^2 \text{ s}^{-1}$, which implies a Reynolds number $R_\epsilon = \infty$ and $R_m \approx 100$, respectively. The Reynolds numbers slightly vary in the box from $R_m = 89$ –125, because both the Alfvén speed and the rotational velocity are functions of radius (see Fig. 1, and Eqs. 27 and 28). For these default parameters, the wavelength of the most unstable MRI mode ranges from $\lambda_{\text{MRI}} = 0.314$ –0.385 km, and the corresponding velocity channels and the magnetic field channels form (for a rotational shear $q = 1.25$) at an angle, $\phi_v = 44.4$ –44.6° and $\phi_b = 134.7$ –134.8°, respectively (see Eqs. (29) and (30)). These angles differ from those in ideal MHD ($\phi_v = 45^\circ$ and $\phi_b = 135^\circ$) only very little.

In all simulations presented below the initial magnetic field has only a uniform component in z direction, as defined in Eq. (8). This field geometry is a popular choice in MRI simulations, (see, e.g. BH91; Hawley & Balbus 1991; Sano & Inutsuka 2001; Obergaulinger et al. 2009), since the vertical component is the most important one for the development of the instability (cf. Balbus & Hawley 1998). Another common choice is a so-called *zero net flux* configuration (see, e.g. Fromang et al. 2007; Fromang & Papaloizou 2007; Obergaulinger et al. 2009), in which the magnetic field has a sinusoidal radial dependence, i.e. $\mathbf{b} \propto \hat{\mathbf{z}} \sin(k_r r)$, where k_r is chosen in such a way that an integer number of wavelengths fits the computational domain. Thus, $k_r = 2\pi n/L_r$ with n being a natural number.

The value of the initial magnetic field amplitude, b_{0z} , requires

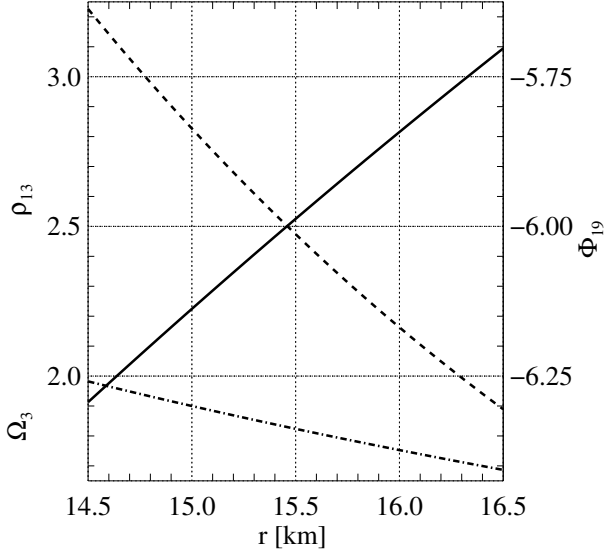


Figure 1. Hydrostatic structure of the initial models. The diagram shows the gravitational potential $\Phi_{19} = \Phi/(10^{19} \text{ erg cm}^{-3})$ (solid line, right ordinate), the density $\rho_{13} = \rho/(10^{13} \text{ g cm}^{-3})$ (dashed line, left ordinate), and the angular velocity $\Omega_3 = \Omega/(10^3 \text{ s}^{-1})$ (dash-dotted line, left ordinate). The entropy profile of this specific model is assumed to be flat.

some further comments. According to state-of-the-art stellar evolution calculations the pre-collapse magnetic field for the most strongly magnetised progenitors is less than about 10^9 G (Heger et al. 2005). During the collapse phase the magnetic field can be amplified by compression by two orders of magnitude to $\approx 10^{11} \text{ G}$ (Meier et al. 1976). From Eq. (24), which is valid in ideal MHD, we estimate that for the PNS the wavelength of the fastest-growing MRI mode is

$$\lambda_{\text{MRI}} \approx 70 \text{ cm} \left(\frac{b_{0z}}{10^{11} \text{ G}} \right) \left(\frac{\rho}{2.5 \times 10^{13} \text{ g cm}^{-3}} \right)^{-1/2} \left(\frac{\Omega}{1900 \text{ s}^{-1}} \right)^{-1}. \quad (47)$$

For the typical Reynolds numbers used in our simulations ($R_e = R_m \approx 100$) the wavelength of the fastest-growing mode is $\approx 1.5\%$ longer (and the growth rate $\approx 1.6\%$ lower) than the one in ideal MHD.² Assuming that 10 zones per MRI channel are needed to resolve it properly, a simulation with $b_{0z} = 10^{11} \text{ G}$ would require a resolution of the order of 10^5 zones per dimension, which is already unaffordable in 2D. One could reduce the cost by using a smaller computational domain, but the high rotational and sound speeds ($v_\phi \approx c_s \approx 3 \times 10^9 \text{ cm s}^{-1}$) would still limit the timestep to $\Delta t \approx 3 \times 10^{-8} \text{ ms}$, i.e. almost 10^7 iterations would be required to simulate the MRI until its termination at $\approx 15 \text{ ms}$.

Therefore, following Obergaulinger et al. (2009), we use initial magnetic fields which are two orders of magnitude higher ($b_{0z} \approx 10^{13} \text{ G}$) to increase the wavelength of the fastest-growing MRI mode to $\approx 100 \text{ m}$. This reduces the minimum resolution to $\approx 100 \times 400 \times 100$ zones in a $1 \text{ km} \times 4 \text{ km} \times 1 \text{ km}$ box, and the number of iterations to less than 10^5 .

² We obtained these values by plotting $\gamma_{\text{mri}}(k_{\text{mri}})$ (for given $\Omega, q, c_{\text{Az}}, \eta$, and ν) using the expression from PC08 and determining the maximum γ_{MRI} and its location, k_{MRI} , graphically.

We pay attention to choose the values of the initial magnetic field strength such that an integer number of channels of the fastest-growing MRI mode fits into the computational domain. In this way this mode fulfils the periodic boundary conditions imposed in z direction. Otherwise, the fastest-growing mode could be artificially suppressed by an unfavourable box size. Rembiasz (2013) showed in test simulations that if, e.g. a box of size $2.5\lambda_{\text{MRI}}$ in z direction is used, usually three MRI channels form. Either all three of them have a wavelength smaller than λ_{MRI} or he finds a combination of larger and smaller channels. In any case, the MRI developed at a rate which was lower than theoretically expected.

To trigger the MRI we impose an initial velocity perturbation on the background velocity profile (defined by Eq. 7) of the form

$$\mathbf{v}_1 = \Omega r [\{\delta_r \mathcal{R}_r(r, \phi, z) + \epsilon \sin(k_z z)\} \hat{\mathbf{r}} + \{\delta_\phi \mathcal{R}_\phi(r, \phi, z)\} \hat{\boldsymbol{\phi}} + \delta_z \mathcal{R}_z(r, \phi, z) \hat{\mathbf{z}}], \quad (48)$$

where $\mathcal{R}_r(r, \phi, z)$, $\mathcal{R}_\phi(r, \phi, z)$, and $\mathcal{R}_z(r, \phi, z)$ are random numbers in the range $[-1, 1]$, δ and δ_r are the perturbation amplitudes, k_z is the radial perturbation wavenumber, and ϵ is the amplitude of the sinusoidal perturbation. If not otherwise written, $k_z = k_{\text{MRI}}$, $\delta_r = 10^{-6}$, $\delta = 10^{-5}$, and $\epsilon = 2 \times 10^{-6}$. Obergaulinger et al. (2009) used a similar prescription for the initial perturbation, except that the sinusoidal part was not present in their case, i.e. $\epsilon = 0$. We find that the sinusoidal term is more robust in exciting MRI modes from small perturbations, which are sometimes suppressed by numerical effects if only random perturbations are imposed (see Rembiasz 2013).

4 RESULTS

4.1 2D simulations

4.1.1 Termination in 2D

Imposing axisymmetry severely limits the number of modes that can grow in 2D simulations. While the fastest-growing MRI mode, which is an axisymmetric one, can freely develop in such simulations, the dominant parasitic instabilities, which for $R_m > 1$ are non-axisymmetric KH modes, are suppressed (Pessah 2010). Hence, among axisymmetric secondary instabilities the fastest-growing modes are of TM rather than KH type. This even holds for simulations with a very low or even a vanishing physical resistivity, as discussed by (Obergaulinger et al. 2009). These authors performed extensive studies of the MRI by means of local 2D ideal MHD simulations. Their simulations confirmed the instability criteria and the growth rates of the MRI for the flow regimes relevant to core collapse supernovae. They also found that the growth of the MRI is terminated by a tearing mode (TM) instability developing because of the unavoidable presence of a numerical resistivity in (even ideal) finite-volume MHD codes.

Figure 2 summarizes the evolution of an axisymmetric model simulated with a resolution of $N_r = N_z = 100$ zones. We performed appropriate convergence studies to ensure that the MRI is properly resolved at this grid resolution (see Rembiasz 2013, for details). The *top left* panel displays the time evolution of the absolute value of the volume-averaged Maxwell stress component

$$\mathcal{M}_{r\phi} \equiv \frac{\left| \int b_r b_\phi dV \right|}{V}, \quad (49)$$

where V is the volume of the computational domain. The other

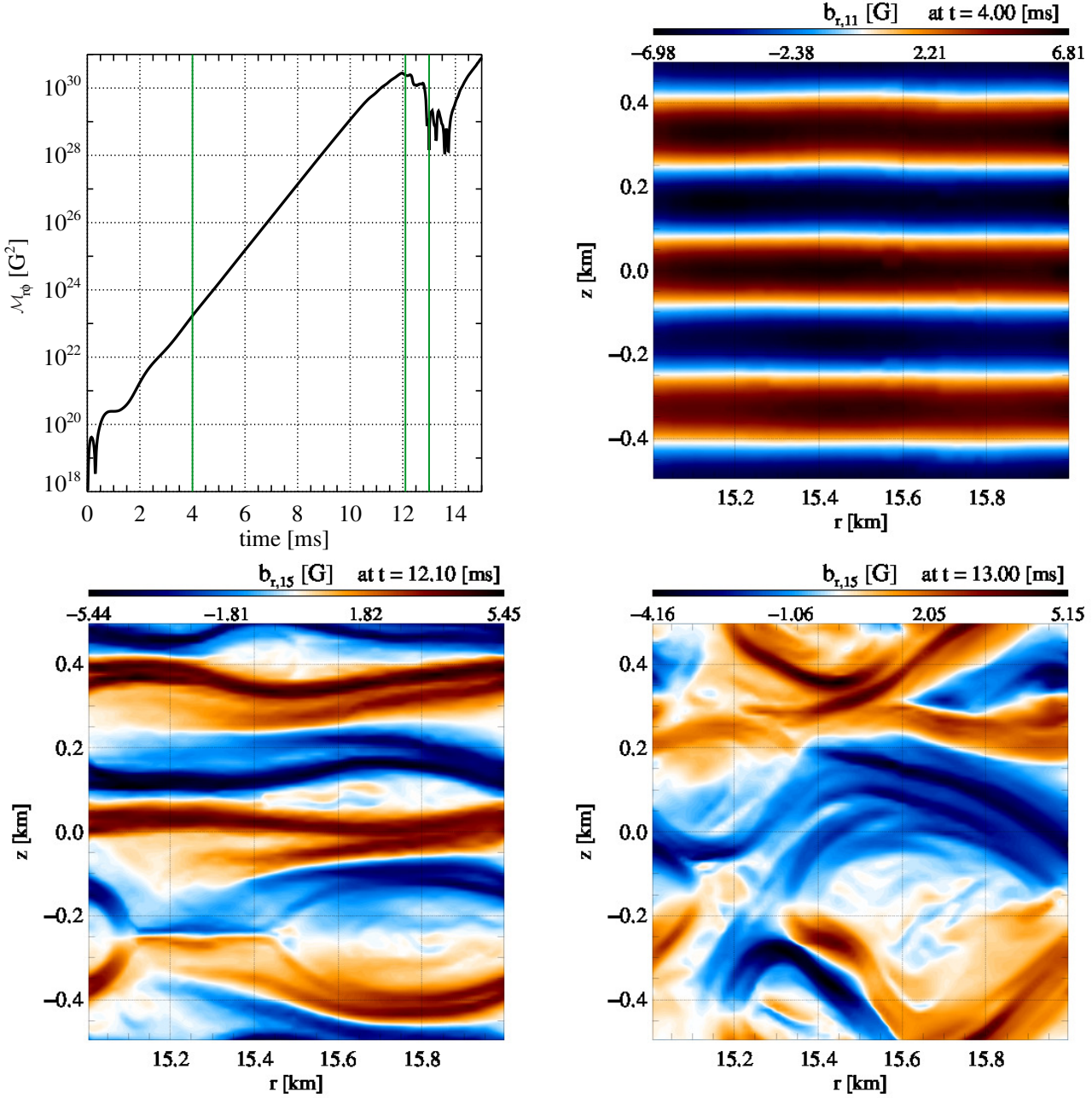


Figure 2. Axisymmetric (2D) MRI simulation in which the instability is terminated by TMs. Top left: Time evolution of the absolute value of the volume averaged Maxwell stress component $\mathcal{M}_{r\phi}$ Eq. (49). The three green vertical lines mark the times corresponding to the snapshots shown in the other three panels, which display the structure of the radial magnetic field at $t = 4$ ms (top right), $t = 12.1$ ms (bottom left), and $t = 13$ ms (bottom right), respectively.

three panels display the colour encoded value of the radial component of the magnetic field in the $r - z$ plane at three different times.

From the initial velocity perturbations (see Eq. 48), three MRI channels have formed at $t = 4$ ms (top right panel) that grow exponentially with time at a constant rate (top left panel). A linear fit of $\log \mathcal{M}_{r\phi}(t)$ in the time interval $t \in [6, 8]$ ms gives $\gamma_{\text{MRI}} = 1127 \text{ s}^{-1}$. This value is consistent with the local linear analysis, Eq. (25), which predicts values of γ_{MRI} varying from 1087 s^{-1} to 1175 s^{-1} within the box boundaries because of its dependence on $\Omega(r)$.

At $t = 12$ ms, the Maxwell stress reaches a value of $\mathcal{M}_{r\phi} =$

$2.78 \times 10^{30} \text{ G}^2$ and the MRI growth is terminated by parasitic instabilities. We note that in 2D simulations, the stress at termination is highly sensitive to the initial random perturbation imposed in the simulation. Performing several realizations of the same simulation, with different seeds for the random number generator, we obtained a Maxwell stress at the termination varying from $\mathcal{M}_{r\phi} = 2.19 \times 10^{30} \text{ G}^2$ to $\mathcal{M}_{r\phi} = 4.69 \times 10^{30} \text{ G}^2$ (see Rembiasz 2013, for details). As we discuss in the next section, we do not observe this large scatter in our 3D simulations.

The colour map of the radial component of the magnetic field exhibits several X points at $t = 12.1$ ms (bottom left panel),

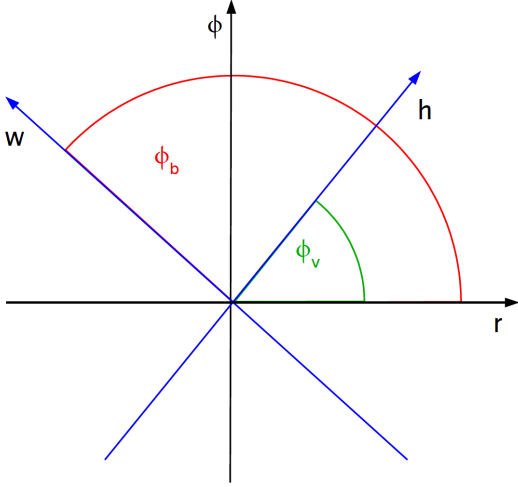


Figure 3. Relation between the (not necessarily orthogonal) coordinates (h, w) defined by Eqs. (50) and (51) and the cylindrical coordinates (r, z) . The angles ϕ_v and ϕ_b are given by Eqs. (29) and (30), respectively. Compare with Fig. 2 of PC08.

where field lines reconnect. These X points are located at $(r, z) = (15.2, 0.4)$, $(16, 0.1)$, and $(15.2, -0.3)$ km, respectively. There are also three O points recognisable in the centres of magnetic islands located at $(r, z) = (15.5, 0.4)$, $(15.7, 0.1)$, and $(15.8, -0.3)$ km, respectively. These patterns indicate MRI termination by TM rather than by KH instabilities. Shortly afterwards, at $t = 13$ ms (*bottom right panel*), the channel modes have been destroyed and MHD turbulence sets in.

These results, which are qualitatively similar to those found by Obergaulinger et al. (2009), confirm that in axisymmetric models the MRI is artificially terminated by TMs, which would grow slower than KH instabilities in 3D models.

4.2 3D simulations

4.2.1 Termination in 3D

According to predictions of Pessah (2010), in general, the fastest-growing KH instabilities should develop along the velocity channels, i.e. $\phi_{\text{KH}} = \phi_v$, whereas the fastest TM should grow along the magnetic field channels, i.e. $\phi_{\text{TM}} = \phi_b$. As these channels define two important directions in the horizontal (r, ϕ) plane, we will sometimes use in the following discussion another coordinate system (h, w, z) , the axes h and w being aligned with the velocity and magnetic field channels, respectively. The (h, w) coordinates and the (r, ϕ) cylindrical coordinates are related through the following coordinate transformation (Fig. 3)

$$\hat{h} = \hat{r} \cos \phi_v + \hat{\phi} \sin \phi_v, \quad (50)$$

$$\hat{w} = \hat{r} \cos \phi_b + \hat{\phi} \sin \phi_b, \quad (51)$$

where the angles ϕ_v and ϕ_b are given by Eqs. (29) and (30), respectively.³ For $R_e = R_m$, the axes h and w are orthogonal, i.e. during the phase of exponential growth of the MRI $b_h = 0$ and $v_w = 0$.

³ This naming convention differs from that of Latter et al. (2009) and Pessah (2010) who used \mathbf{h} to denote vectors (or their components) in the (r, ϕ) plane.

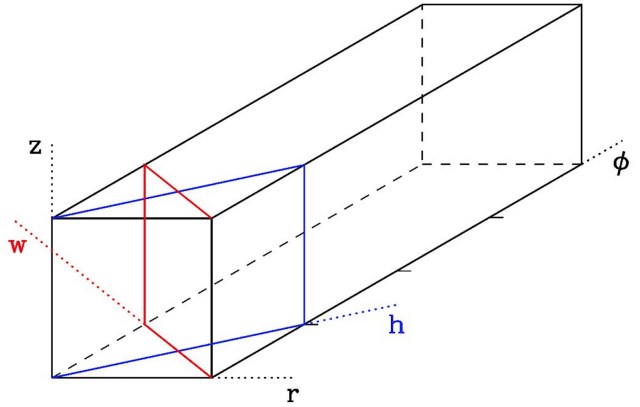


Figure 4. Sketch of the computational domain of size $1 \times 4 \times 1$ km, which was used to simulate models #5 to #8 and #10 (see Table 1) together with two cuts corresponding to the (h, z) plane (blue) and the (w, z) plane (red) used to display some results of model #7 in Fig. 8. Note that the computational volume is actually bent in ϕ direction and the two cuts are no planes but curved surfaces in cylindrical coordinates.

Figure 3 depicts the horizontal plane in both coordinate systems. The channel angles are set to $\phi_v = 45^\circ$ and $\phi_b = 135^\circ$, which corresponds to the ideal MHD limit. In general, the vectors \hat{h} and \hat{w} are not orthogonal to each other, and their exact orientation depends on the Reynolds numbers. For example, in the limit $R_e \rightarrow \infty$ and $R_m \rightarrow 0$, one has $\hat{h} \parallel \hat{r}$ and $\hat{w} \parallel \hat{\phi}$, i.e. $\phi_v = 0^\circ$ and $\phi_b = 90^\circ$ (PC08).

For the values of the Reynolds numbers used in our simulations, i.e. $R_e = \infty$, $R_m \approx 100$, and $R_e = R_m \approx 100$, we expect the channels to be oriented along $\phi_v = 44.4\text{--}44.6^\circ$, $\phi_b = 134.7\text{--}134.8^\circ$, $\phi_v = 44.3\text{--}44.5^\circ$, and $\phi_b = 134.5^\circ$, respectively. These angles differ only little from those of the ideal MHD case. Hence, in either case, the fastest-growing KH mode should develop at an angle $\phi_p = \phi_{\text{KH}} \approx 44.5^\circ$, where ϕ_p denotes the angle at which the dominant parasitic instability develops. Depending on the initial conditions, one either has $\phi_p = \phi_{\text{KH}}$ or $\phi_p = \phi_{\text{TM}}$. In 2D axisymmetric simulations, the only allowed angle is $\phi_p = 0^\circ$.

We studied the termination process in a number of 3D simulations, varying the size and aspect ratio of the computational domain, and the grid resolution (see Tab. 1 for the list of models). The default simulation box has a size of $L_r \times L_\phi \times L_z = 1 \text{ km} \times 4 \text{ km} \times 1 \text{ km}$, as shown in Fig. 4, which also depicts two cuts corresponding to the (h, z) and (w, z) planes. We note that the computational volume is actually bent in ϕ direction and the two cuts are not planes but curved surfaces in cylindrical coordinates. However, we will call them planes for simplicity.

We begin the discussion of our results with model #7 (see Tab. 1), which we simulated in the default box resolved with $100 \times 400 \times 100$ zones in r , ϕ , and z direction, respectively. Except for the third space dimension, the initial conditions and the parameters of this 3D model are identical to those of the axisymmetric model discussed in Sec. 4.1. As illustrated by the time evolution of the Maxwell stress (Fig. 5), the MRI grows exponentially with time at the same rate as in the 2D model ($\gamma_{\text{MRI}} = 1127 \text{ s}^{-1}$) until saturation, which occurs a bit earlier than in the 2D model at $t = 11.2$ ms.

Figure 6 shows the 3D structure of the radial component of the magnetic field at six distinct times (marked by vertical lines in Fig. 5). Magnetic field perturbations grow in the form of three axisymmetric channels (*upper left panel*), which are perturbed in turn

Table 1. Overview of our 3D MRI simulations, which were all performed with the initial parameters chosen in such a way that $\lambda_{\text{MRI}} \approx 0.333 \text{ km}^*$. The columns give the model identifier, the magnetic field strength, the hydrodynamic and magnetic Reynolds numbers (R_e and R_m , respectively), * the size of the computational domain, the resolution, the number of grid cells per MRI wavelength, the measured MRI growth rate, the volume-averaged Maxwell stress at termination, the azimuth angle at which the parasitic instability develops, and its horizontal wavelength (i.e. in the (r, ϕ) plane) measured at $t = 11 \text{ ms}$ and $t = 12.5 \text{ ms}$ for KH instabilities and TMs, respectively. The azimuth angle and the horizontal wavelength are determined with about a 9° and 10% accuracy, respectively (see also Fig. 12). The final column gives the type of the instability. For models 19 and 20, we were unable to identify the type of the parasitic instability terminating the growth of the MRI.

#	b_{0z} [10^{13} G]	R_e	R_m	box size ($r \times \phi \times z$) [km]	resolution ($r \times \phi \times z$)	zones per channel	$\gamma_{\text{MRI}} [\text{s}^{-1}]$	$\mathcal{M}_{r\phi}$ [10^{30} G^2]	$\phi_p [^\circ]$	$\frac{\lambda_p}{\lambda_{\text{MRI}}}$	term. instab.
1	4.6	∞	∞	$1 \times 4 \times 1$	$100 \times 400 \times 100$	33	1137	0.96	45	0.94	KH
2	4.6	∞	100	$1 \times 1 \times 0.333$	$24 \times 24 \times 8$	8	1104	0.79	45	1.5	KH
3	4.6	∞	100	$1 \times 1 \times 0.333$	$30 \times 30 \times 10$	10	1122	1.3	44	1.2	KH
4	4.6	∞	100	$1 \times 1 \times 0.333$	$48 \times 48 \times 16$	16	1130	1.1	47	1.1	KH
5	4.6	∞	100	$1 \times 4 \times 1$	$60 \times 240 \times 60$	20	1126	1.1	44	0.92	KH
6	4.6	∞	100	$1 \times 4 \times 1$	$76 \times 304 \times 76$	25	1127	1.0	47	0.99	KH
7	4.6	∞	100	$1 \times 4 \times 1$	$100 \times 400 \times 100$	33	1127	0.93	44	0.85	KH
8	4.6	∞	100	$1 \times 1 \times 1$	$100 \times 100 \times 100$	33	1127	0.93	47	0.95	KH
9	4.6	∞	100	$1 \times 1 \times 0.333$	$100 \times 100 \times 34$	34	1127	0.93	47	0.77	KH
10	4.6	∞	100	$1 \times 4 \times 1$	$200 \times 800 \times 200$	67	1127	0.73	44	0.70	KH
11	4.6	∞	100	$1 \times 1 \times 0.333$	$400 \times 400 \times 134$	134	1128	0.73	45	0.69	KH
12	4.6	100	100	$1 \times 1 \times 0.333$	$100 \times 100 \times 34$	34	1120	0.90	44	0.85	KH
13	4.6	100	100	$1 \times 0.8 \times 0.333$	$100 \times 80 \times 34$	34	1120	0.92	44	0.80	KH
14	4.6	100	100	$1 \times 0.6 \times 0.333$	$100 \times 60 \times 34$	34	1120	1.0	43	0.96	KH
15	4.6	100	100	$1 \times 0.4 \times 0.333$	$100 \times 40 \times 34$	34	1120	0.97	43	0.80	KH
16	4.6	100	100	$1 \times 0.3 \times 0.333$	$100 \times 30 \times 34$	34	1120	1.1	52	0.70	KH
17	4.6	100	100	$1 \times 0.2 \times 0.333$	$100 \times 20 \times 34$	34	1120	4.5	-	-	TM
18	4.6	100	100	$1 \times 0.1 \times 0.333$	$100 \times 10 \times 34$	34	1120	4.9	-	-	TM
19	0.325	∞	0.1	$1 \times 1 \times 0.333$	$100 \times 100 \times 34$	34	80	0.0020	-	-	?
20	0.163	∞	0.05	$1 \times 1 \times 0.333$	$100 \times 100 \times 34$	34	34	0.0011	-	-	?

* Note that λ_{MRI} , R_e , and R_m are not uniform throughout the computational domain, but vary by $\approx 20\%$ (see Sec. 3.4 for details).

by secondary instabilities that become recognisable only shortly before the MRI is terminated at $t = 11.2 \text{ ms}$. The sequence of snapshots around this time (*upper middle* to *bottom middle*) demonstrates that non-axisymmetric parasitic modes are responsible for MRI termination. After exponential growth of the magnetic field has ended, the simulation volume is dominated by a small-scale, turbulent magnetic field (*bottom right*). Comparing the structure of the radial magnetic field during MRI termination (Fig. 7), we find profound differences between the 2D model (*left-hand* panel) and the 3D model (*right-hand* panel). The 2D model exhibits X and O points that are characteristic of the TM instability, whereas in the 3D simulation the channel modes bend strongly at the locations of vortex rolls which are a typical feature of the KH instability.

We also studied some geometrical aspects of the parasitic instabilities found in the 3D simulation. For this purpose, we use the (h, w, z) coordinates. Velocity-shear driven KH instabilities should grow fastest in the h direction and dominantly current driven TM along the w axis. To simplify the expressions we performed the coordinate transformation $(r, \phi, z) \rightarrow (h, w, z)$ with $\phi_v = 45^\circ$ and $\phi_b = 135^\circ$ instead of the theoretically expected angles $\phi_v = 44.5^\circ$ and $\phi_b = 134.8^\circ$, which does not affect our qualitative analysis, however.

Figure 8 shows the distribution of the magnetic field components b_h (*left-hand panels*) and b_w (*right-hand panels*) in two-dimensional cuts through the computational domain of the 3D model #7 shortly before MRI termination. The component b_h is considerably smaller than the component b_w . This is consistent

with the theoretical expectation for an MRI channel whose magnetic field should grow in the w direction ($\phi_b = 135^\circ$) and vanish in the perpendicular h direction ($\phi = 45^\circ$). Close to termination, the MRI channels are strongly perturbed and vortex rolls begin to form in the h direction (*upper panels*). This indicates that KH instabilities developing along the velocity channels (i.e. in the h direction) are responsible for the disruption of the MRI channels. In the w direction (i.e. along the magnetic field channels separated by current sheets in which TM could develop), the channels remain almost unperturbed. Only box-size structures appear which are most likely a consequence of the radial boundary conditions imposed in our simulations (see Sec. 3.3). Although we cannot discard the presence of sub-dominant TM in this projection, it is clear that TM do not play a dominant role in the termination process, which can be understood completely in terms of parasitic KH instabilities.

Before we proceed further we take another look at the spatial structure of b_r during MRI termination at $t = 11.1 \text{ ms}$, which is illustrated in Fig. 9. In the upper panel depicting b_r in a (ϕ, z) cut at $r = 16 \text{ km}$ (this cut corresponds to the outer radial boundary of the computational domain shown in the upper right panel of Fig. 6), one can recognize vortex rolls developing along the MRI channels. From the middle panel, which shows the distribution of b_r in the $(r - \phi)$ plane at $z = 0.335 \text{ km}$, one could determine the horizontal wavelength λ_p and the angle at which parasitic instabilities develop ($\phi_p \approx 45^\circ$). However, we can obtain these quantities much more accurately using Fourier transforms (see next subsection). The bottom panel provides another view of the structure of b_r . By showing

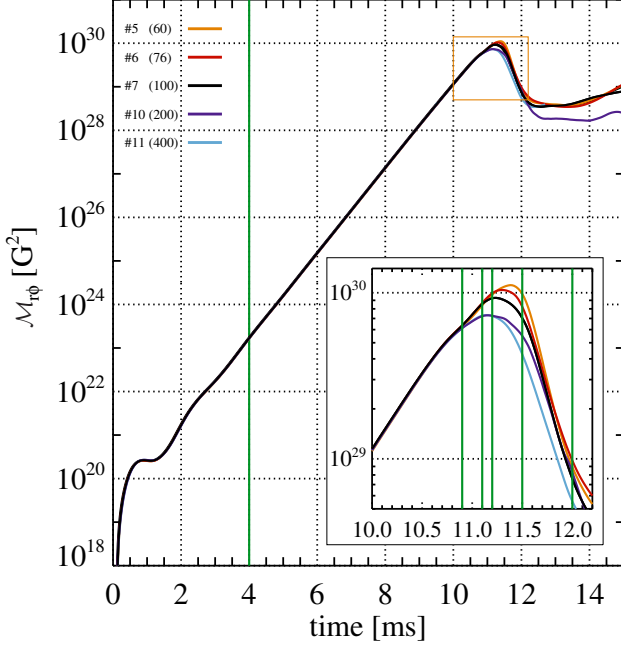


Figure 5. Evolution of the volume-averaged Maxwell stress component $\mathcal{M}_{r\phi}$ for the 3D models #5 (orange), #6 (red), #7 (black), #10 (violet), and #11 (blue; run only until $t = 12$ ms). Up to $t \approx 10.5$ ms, the models give almost identical results, differences being only visible around termination (see inset). Vertical lines indicate the times of the snapshots displayed for model #7 in Fig. 6. For a better readability of the figure, the vertical lines around MRI termination are only displayed in the inset.

a part of both the (h, z) cut and the (w, z) cut, it illustrates in which direction parasitic instabilities develop. We note that the (h, z) and (w, z) cuts shown in Figs. 9 and 8 are different.

4.2.2 Fourier analysis

In order to confront the theoretical expectations with our numerical results, we have calculated spatial discrete 3D Fourier transforms of the magnetic field components b_α with $\alpha \in r, \phi$ at a given time using a fast Fourier Transform (FFT) algorithm. We denote the complex FFT coefficients as a_α . The power spectral density is proportional to $|a_\alpha|^2$, which is a measure of the average magnetic field energy density of the component b_α in Fourier space. We chose the components b_r and b_ϕ for the analysis, because they contain the information about both the MRI channel flows and the parasitic instabilities. We are particularly interested in determining the wavevectors, $\mathbf{k} = (k_r, k_\phi, k_z)$, of the dominant modes, which have the largest amplitudes in the Fourier space. We expect that MRI channel flows appear as structures with a wavevector

$$\mathbf{k}_{\text{mri}} = (0, 0, k_{\text{mri}}), \quad (52)$$

whose modulus is maximum for the fastest-growing mode, k_{mri} .

Parasitic instabilities develop in the whole Fourier space, whereas the MRI does not contribute to modes with finite k_r and k_ϕ , but $k_z = 0$. Hence, parasitic instabilities are expected to produce a characteristic signature with wavevectors

$$\mathbf{k}_p = (k_r, k_\phi, 0), \quad (53)$$

which should be distinguishable from the MRI signature. The maximum Fourier amplitude should be attained for the wavevector of the fastest-growing parasitic mode.

The analysis of model #7 reveals that the Fourier amplitude along the line $k_r = k_\phi = 0$ peaks at $k_z = 18.8 \text{ km}^{-1}$, which corresponds to the wavelength of the fastest-growing MRI mode, $\lambda_{\text{MRI}} \approx 0.333 \text{ km}$ of this model. The latter result holds for all our simulations during the phase of exponential growth of the MRI. The Fourier amplitudes in the plane $k_z = 0$, displayed for three different times for model #7 in Fig. 10, show a power excess which peaks at $(k_r, k_\phi) \approx (0.7, 0.7) \text{ km}^{-1}$. The location of this maximum barely changes with time, while the amplitudes of the Fourier coefficients increase relative to those at $(0, 0, k_{\text{MRI}})$. This result is consistent with a super-exponential growth of parasitic instabilities. In addition, as we will demonstrate below, the behaviour of the Fourier amplitude in the $k_z = 0$ plane is consistent with the development of parasitic KH instabilities feeding off the MRI channels.

The average magnetic energy density of the field component b_α can be computed from the Fourier amplitudes as

$$e_{\text{mag},\alpha} = \frac{1}{2} \sum_{l=-N_r/2}^{N_r/2} \sum_{m=-N_\phi/2}^{N_\phi/2} \sum_{n=-N_z/2}^{N_z/2} |a_\alpha(k_l, k_m, k_n)|^2, \quad (54)$$

where

$$(k_l, k_m, k_n) = \left(\frac{2\pi l}{L_r}, \frac{2\pi m}{L_\phi}, \frac{2\pi n}{L_z} \right). \quad (55)$$

Similarly, we can estimate the average magnetic energy density of the MRI channels or parasitic instabilities restricting the summation to locations in Fourier space relevant for each kind of instability. Therefore, we define

$$e_{\text{MRI},\alpha} = |a_\alpha(0, 0, k_{\text{MRI}})|^2, \quad (56)$$

$$e_{p,\alpha} = \frac{1}{2} \sum_{l=-N_r/2}^{N_r/2} \sum_{m=-N_\phi/2}^{N_\phi/2} |a_\alpha(k_l, k_m, 0)|^2, \quad (57)$$

as proxies for the average magnetic field energy density associated with these instabilities. In case of the MRI, the Fourier amplitudes are distributed along the line $k_r = k_\phi = 0$, i.e. $e_{\text{MRI},\alpha}$ should be a good estimator. However, in the case of the parasitic modes, $e_{p,\alpha}$ contains not all contributions to the energy density and thus provides only a lower bound of the energy density associated with the parasitic instabilities.

Fig. 11 shows the time evolution of the magnetic energy density for both the MRI and the parasitic instabilities. The behaviour of $e_{\text{MRI},\alpha}$ is very similar to the time evolution of the Maxwell stress (see Fig. 5). It is characterized by an exponential growth with the same growth rate as for the Maxwell stress $\mathcal{M}_{r\phi}$, and a termination point associated with the disruption of the MRI channel flows. The average magnetic energy density $e_{p,\alpha}$ of the parasites starts to grow super-exponentially at $t \approx 9$ ms from a value of about 8 orders of magnitude smaller than that of the MRI. At termination, the magnetic energy density of the parasites amounts to, at least, 6% of the magnetic energy density of the MRI.

To determine the wavevector of the fastest-growing parasitic instability, we search for the maximum Fourier amplitude with $k_z = 0$. For this purpose, it is sufficient to consider only positive components of the wavevector \mathbf{k} . Numerically, we obtain the wavevector by computing the energy-weighted barycenter in the relevant part of Fourier space,

$$k_{p,\alpha} = \frac{\sum_{l=1} \sum_{m=1} |a_\alpha(k_l, k_m, 0)|^2 k_\alpha}{\sum_{l=1} \sum_{m=1} |a_\alpha(k_l, k_m, 0)|^2}, \quad (58)$$

where we limited all summations to those Fourier modes displayed in Fig. 10 to avoid high frequency contaminations. Substituting a_r for a_ϕ does not change the results significantly.

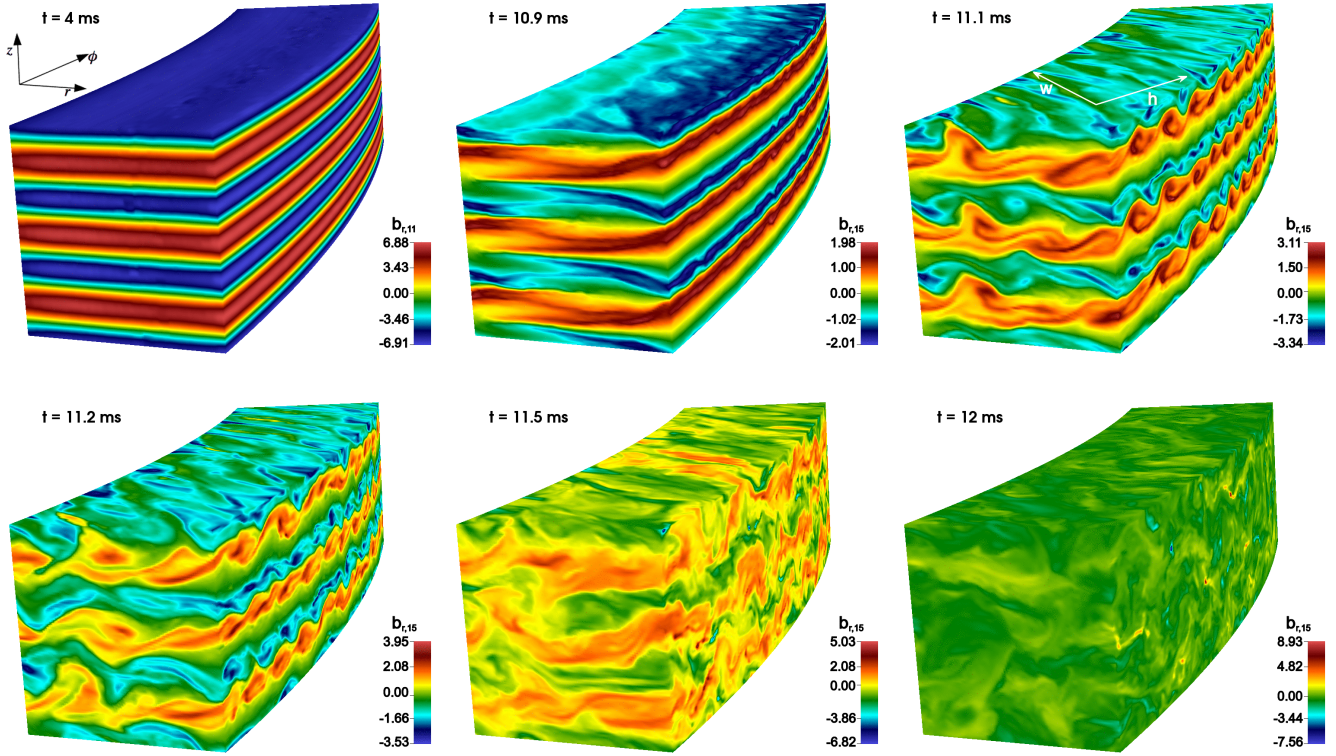


Figure 6. Distribution of the radial component of the magnetic field b_r across the surface of the computational domain for the 3D model #7 at six different times. The times of the snapshot are marked by green vertical lines in Fig. 5.

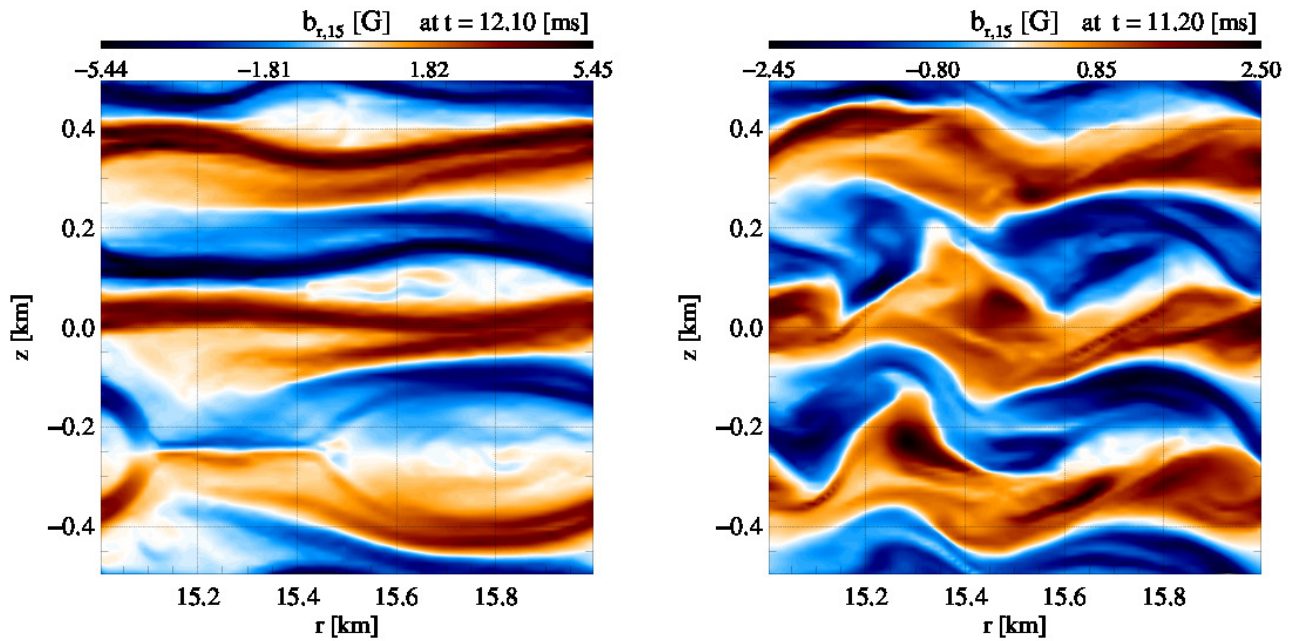


Figure 7. Comparison of the distribution of the radial magnetic field b_r around MRI termination in a 2D (left) and 3D (right) simulation (model #7; cut at $\phi = -2$ km). Note that the two snapshots are taken at different times.

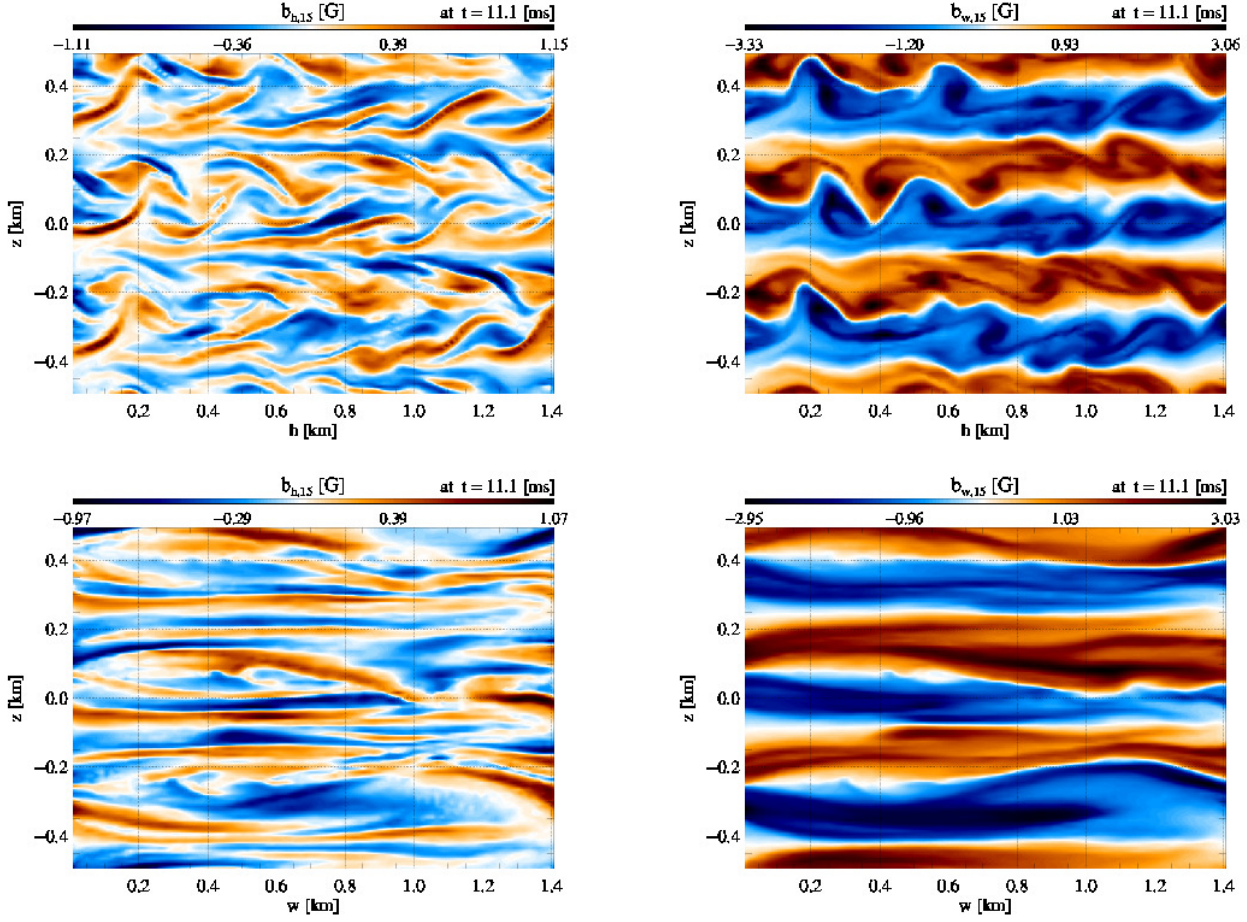


Figure 8. The panels show the distribution of the magnetic field components b_h (left) and b_w (right) in two-dimensional cuts through the computational domain for the 3D model #7 at time $t = 11.1$ ms. The cut directions are perpendicular (top panels; (h, z) cut) and parallel (bottom panels; (w, z) cut) to the direction of the magnetic MRI channels. The locations of the cuts are marked in Fig. 4 in blue and red, respectively.

The values of $k_{p,\alpha}$ obtained from Eq. (58) (white squares in Fig. 10) properly trace the location of the maximum Fourier amplitude. With these values one can compute both the wavelength and the angle of the parasitic instability according to

$$\lambda_p = \frac{2\pi}{\sqrt{k_{p,r}^2 + k_{p,\phi}^2}}, \quad (59)$$

$$\phi_p = \arctan\left(\frac{k_{p,r}}{k_{p,\phi}}\right). \quad (60)$$

Figure 12 shows the time evolution of the wavelength, λ_p , and angle, ϕ_p , of the parasitic instabilities during the late stage of MRI evolution. Before MRI termination, the evolution of the angle is compatible with its theoretically expected behaviour for KH instabilities, i.e. $\phi_p \approx 45^\circ$ (horizontal green line), within the accuracy of the angle determination.⁴ The wavelength differs from its theoretically expected value $\lambda_p \approx 0.56$ km (horizontal blue line) by a factor of ~ 2 . Whether the source of this disagreement is of a numerical origin or results from a limitation of the theoretical approach of Pessah (2010) is beyond the scope of this work.

⁴ The accuracy in the determination of the angle and the wavelength, $\approx 9^\circ$ and $\approx 10\%$ respectively, depends on the accuracy in the determination of \mathbf{k}_p , which is set by the size of the box.

We have performed a similar analysis for all our other simulations. Table 1 gives the values of λ_p and ϕ_p at a representative time before termination (i.e. at 11 ms for models #1 to #16, and at 12.5 ms for models #17 and #18). In the following three subsections, we discuss the influence of different numerical and physical parameters on the values of these two quantities.

4.2.3 Box size

Next, we address whether the size and aspect ratio of the computational domain influences MRI termination (for a somewhat similar study of the post-termination phase, see Bodo et al. 2008). Following Obergaulinger et al. (2009), we simulated models #5, #6, #7, and #10 in a box of (the default) size ($L_r \times L_\phi \times L_z = 1 \text{ km} \times 4 \text{ km} \times 1 \text{ km}$). We performed additional simulations reducing the size of the box in ϕ direction ($1 \text{ km} \times 1 \text{ km} \times 1 \text{ km}$, model #8), and both in ϕ and z direction ($1 \text{ km} \times 1 \text{ km} \times 0.333 \text{ km}$, models #2, #3, #4, #9, and #11). Finally, we computed several models (#12 to #18) where we varied the azimuthal size L_ϕ of the domain (see Table 1).

The main motivation for using a smaller box in some of our simulations was computational cost reduction. In accordance with theoretical predictions of Pessah (2010) for flows with $R_e, R_m \gg 1$, we found that in model #7 parasitic instabilities develop at an an-

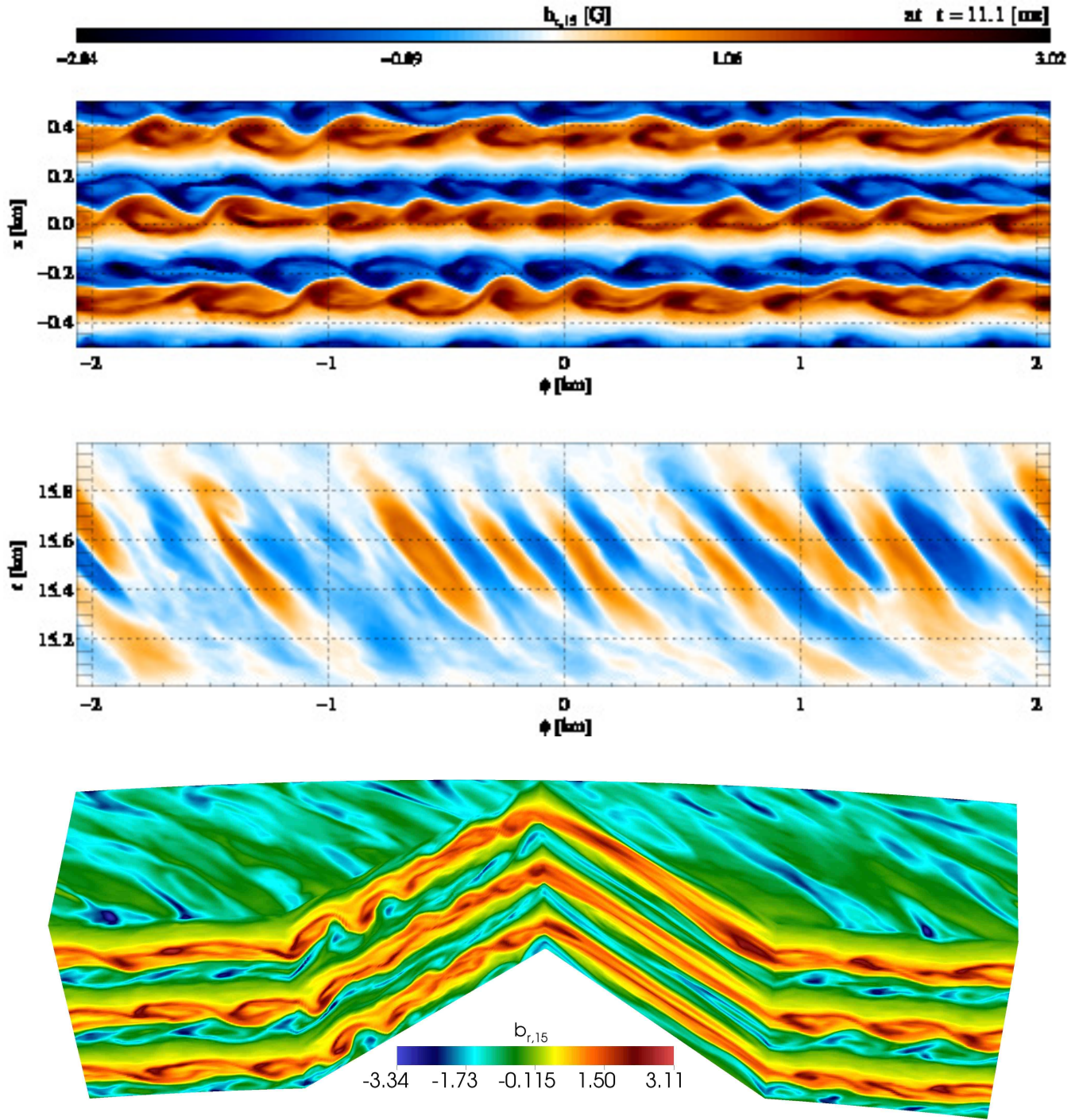


Figure 9. Structure of the radial magnetic field component b_r of the 3D model #7 at $t = 11.1$ ms. *Top:* (z, ϕ) cut at $r = 16$ km. *Middle:* (r, ϕ) cut at $z = -0.09$ km. *Bottom:* 3D view of the surface of the computational domain where some part of it has been removed to show pieces of the (h, z) and (w, z) cuts. Note that these cuts differ from those displayed in Fig. 8.

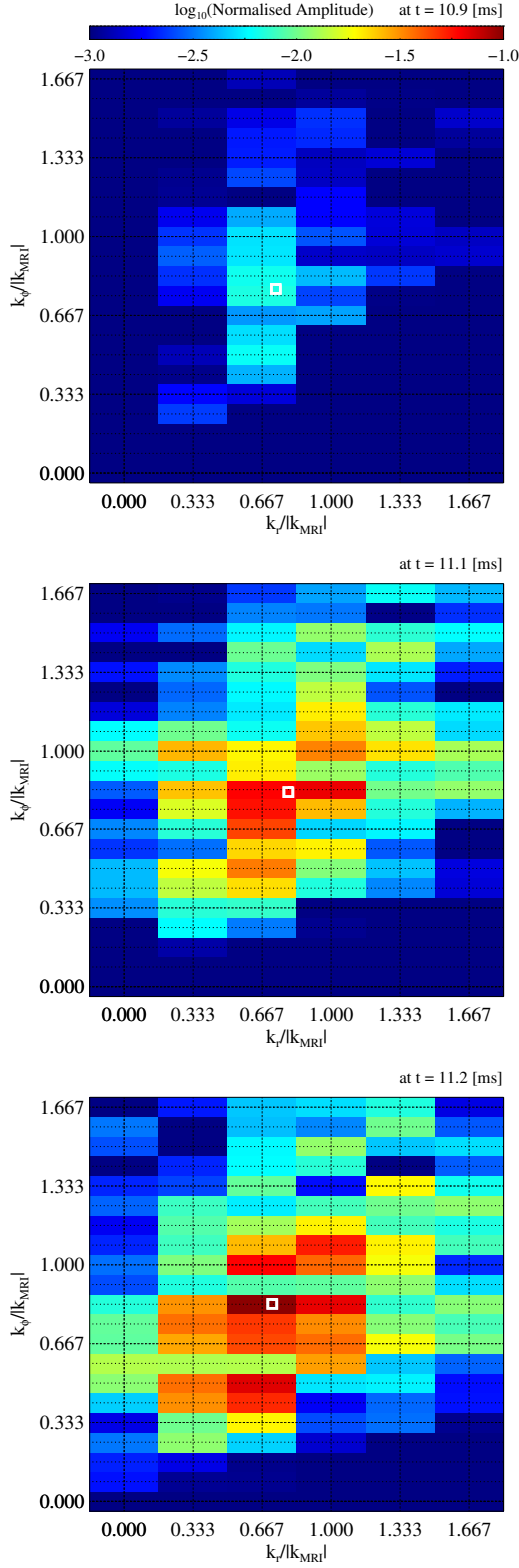


Figure 10. Fourier amplitudes of the radial magnetic field b_r for model #7 at 10.9 ms (top), 11.1 ms (middle), and 11.2 ms (bottom), respectively. The colour coded quantity is the ratio $|a(k_r, k_\phi, 0)|/|a(0, 0, k_{\text{MRI}})|$ of the Fourier amplitude representing parasitic instabilities and the one representing MRI channels. The white square is the location of the energy-weighted barycenter computed with Eq. (58).

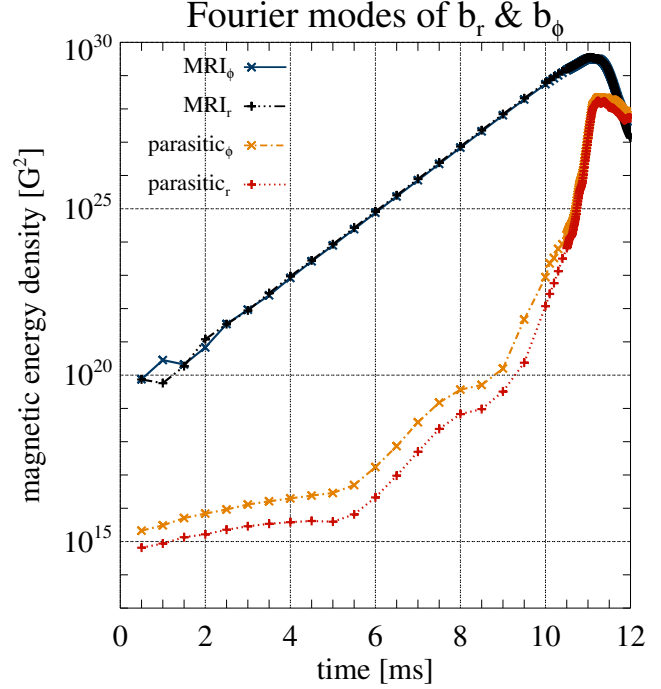


Figure 11. Evolution of the average magnetic energy density associated with the MRI channels ($e_{\text{MRI},\alpha}$) and the parasitic instabilities ($e_{\text{p},\alpha}$) for different components b_α of the magnetic field for model #7.

gle $\phi_p \approx 45^\circ$ (see Fig. 12, and middle panel of Fig. 9). This result suggests that it is unnecessary to use a box elongated in azimuthal direction ($L_\phi > L_r$). Instead, one could rather study the MRI in a box with a horizontal aspect ratio $L_r = L_\phi$ to minimize the volume of the computational domain without affecting the development of parasitic instabilities. To test this hypothesis, we simulated model #8 in a box of size $L_r \times L_\phi \times L_z = 1 \text{ km} \times 1 \text{ km} \times 1 \text{ km}$ using the same spatial resolution as for reference model #7. In both simulations, the Maxwell stress tensor at MRI termination attained the same value, which confirms our expectations.

We can further reduce the computational domain in the vertical direction based on the following observation. In simulations performed with the default box, we chose the magnetic field strength in such a way that three of the fastest-growing MRI modes fit in the computational domain. Thus, it should be possible to reduce the vertical extent of the box by a factor of 3, i.e. $L_z = \lambda_{\text{MRI}} \approx 0.333 \text{ km}$, without hindering the growth of the dominant MRI mode. However, in such a smaller domain parasitic instabilities are restricted to modes having a vertical wavelength equal to the width of an MRI channel (called Type-I modes by GX94), and modes with a longer vertical wavelength (Type-II') are suppressed. Nonetheless, according to the predictions of GX94 and Pessah (2010), in the ideal MHD limit or for $Re, R_m > 1$, the dominant parasitic modes should be (KH modes) of Type-I. Hence, we expect the MRI termination process to be unaltered by a box of smaller vertical size.

To test this theoretical prediction, we simulated model #9 in a box of size $L_r \times L_\phi \times L_z = 1 \text{ km} \times 1 \text{ km} \times 0.333 \text{ km}$ using the same grid resolution as in models #7 and #8. We found that the Maxwell stress tensor reached the same value at MRI termination in all three models. This result not only confirms (given our initial conditions) the termination of the MRI by “Type-I” parasitic modes, which is an important result, but it also justifies the use of a computational

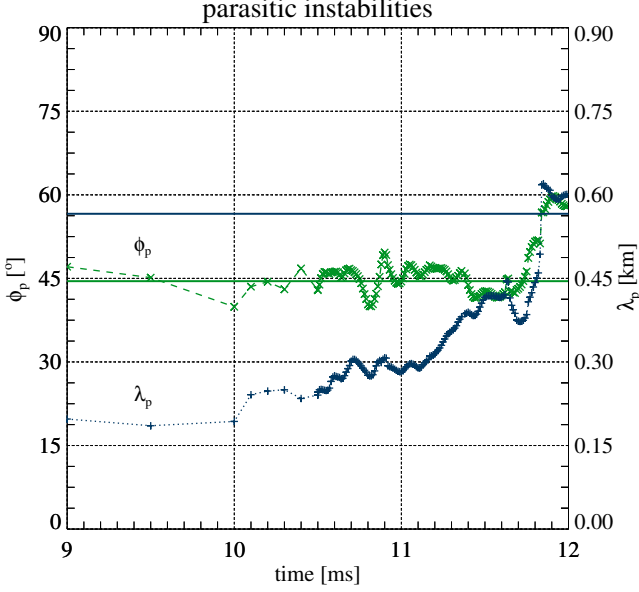


Figure 12. Characteristics of the parasitic instabilities for model #7 during the late stage of MRI evolution. Green crosses and blue diamonds depict the angle, ϕ_p , and the wavelength, λ_p , of the parasites, respectively. Horizontal solid lines show the corresponding theoretical values for KH modes that one expects to develop in this simulation.

box with a 12 times smaller volume for studying the MRI termination process. We made use of this fact in our resolution studies (see next subsection).

In Section 4.1, we showed that the MRI is terminated by TMs in axisymmetric 2D simulations. One can also impose axisymmetry in 3D simulations by choosing a box of vanishing azimuthal length, i.e. $L_\phi \rightarrow 0$. Therefore, we expect that for a certain small, but non-zero L_ϕ , KH instabilities should be suppressed even in 3D simulations, and the MRI should be terminated by TM instead. To determine this critical azimuthal box length, we performed a series of simulations varying L_ϕ from 1.0 to 0.1 km (models #12 to #18). Moreover, to investigate the influence of viscosity, we ran these simulations with a non-zero shear viscosity corresponding to a hydrodynamic Reynolds number $Re = 100$. The shear viscosity should change the wavelength of the fastest growing MRI mode, but only by a negligible amount from the numerical point of view (i.e. less than 1%).

As expected, the MRI is terminated by KH instabilities in model #12, which only differs from model #9 by the value of Re . In both simulations, the parasitic instabilities have the same horizontal wavelength, λ_p , and they develop at the same angle ϕ_p within the measurement error. In models #13–#16, the MRI is also terminated by KH instabilities, but the value of the Maxwell stress tensor at termination is somewhat larger. This result can be easily understood: parasitic modes that would grow fastest in a box with $L_\phi = 1$ km are affected (or even suppressed) in narrower boxes, i.e. the MRI can operate a bit longer before it is finally terminated. The smaller the box, the stronger the suppression of the KH modes and the larger the deviation of such quantities as the Maxwell stress at termination from model #12. Finally, in models #17 ($L_\phi = 0.2$ km) and #18 ($L_\phi = 0.1$ km), KH modes are suppressed and the MRI is terminated by TMs, showing similar features as in the 2D simulations described in section 4.1. We note that the Maxwell stress reaches considerably higher values at termination in these models, because TM are growing more slowly. A similar behaviour was ob-

served by Lesaffre et al. (2009) in their mean-field shearing-box simulations of accretion discs. In simulations done in a box of size $L_r = L_\phi = L_z = \lambda_{\text{MRI}}$, KH modes were suppressed and the MRI channels were disrupted by TM, whereas in simulations done in larger boxes in the horizontal directions (i.e. $L_r = L_z = \lambda_{\text{MRI}}$ and $L_\phi = 4\lambda_{\text{MRI}}$, or $L_z = \lambda_{\text{MRI}}$ and $L_r = L_\phi = 4\lambda_{\text{MRI}}$), the MRI was terminated by KH instabilities.

To summarize, MRI termination in models #12–#18 is well explained within the parasite model, and the minimum azimuthal box length for which KH modes are not severely affected by boundary conditions is $L_\phi \approx 0.3$ km $\approx 1\lambda_{\text{MRI}}$.

4.2.4 Influence of grid resolution

To properly resolve MRI termination, one needs to use a resolution that is high enough not only to resolve the MRI channels, but also parasitic instabilities. The latter criterion is more stringent, as parasitic instabilities develop finer structures in vertical direction than MRI channels do (GX94, Pessah 2010).

We explore this issue in a series of simulations performed in the small ($L_r \times L_\phi \times L_z = 1$ km \times 1 km \times 0.333 km; models #2, #3, #4, #9, and #11) and in the default ($L_r \times L_\phi \times L_z = 1$ km \times 4 km \times 1 km; models #5, #6, #7, and #10) computational box. As we have demonstrated in the previous subsection, parasitic instabilities can develop equally well in both computational domains, i.e. the boxes are equally well suited for resolution studies.

In models #2–#4, which were simulated with 8–16 zones per MRI channel in the vertical direction, we observe differences already during the phase of exponential growth. First, channel modes emerge ≈ 2 ms later than in the other better resolved simulations. Secondly, the channel modes somewhat differ from the analytic solution, i.e. some imperfections develop on channels which are of numerical and not physical origin. Thirdly, the MRI growth rate measured with the help of $\mathcal{M}_{r\phi}$ slightly fluctuates during the phase of exponential growth. These fluctuations of the order of a few percent can be explained by the fact that the above mentioned imperfections also contribute to $\mathcal{M}_{r\phi}$.

In models #5–#11, which were simulated with at least 20 zones per MRI channel, the channel modes appear roughly at the same time and grow at the same constant rate during the phase of exponential growth. Based on these observations, we conclude that 20 zones per MRI channel are sufficient to resolve the phase of exponential growth with the MP9 scheme (but more zones will be required for lower order reconstruction schemes). This result is consistent with previous estimations of the numerical viscosity and resistivity of the code done by Rembiasz (2013). With the help of tests involving Alfvén wave propagation and TM instabilities, he determined scaling laws for the numerical viscosity and resistivity of the code as a function of resolution and initial conditions. Given our numerical setup, the numerical viscosity and resistivity of the code are $< 10^7$ cm²s^{−1}, if the relevant length scale is covered by at least 20 zones (see also section 4.2.5.1).

To investigate the nature of the parasitic instabilities that are responsible for quenching the MRI, we used both Fourier analysis and the local magnetic field structure during MRI termination. In models #2 to #11, we find parasitic instabilities of KH type developing at an angle consistent with $\phi_p = 45^\circ$ independent of resolution. The horizontal wavelength of the parasitic modes ranges from $\lambda_p \approx 0.50$ km in the coarsest resolved model #2 to $\lambda_p \approx 0.23$ km in the best resolved models #10 and #11.

Remarkably KH instabilities develop even in model #2, although it was simulated with the coarsest grid which noticeably

affects the structure of the channel modes. Their identification was not straightforward, however. From the patterns recognizable in the magnetic field structure during MRI termination, one can exclude TM and other obvious numerical artefacts, e.g., arising from imperfect boundary conditions. We also find patterns resembling underresolved vortex rolls which we attribute to KH modes, although without the help of Fourier analysis, our experience gained from observing similar patterns in better resolved simulations, and most importantly a theoretical model (GX94; Pessah 2010), this identification would have been impossible.

The value of the Maxwell stress at MRI termination depends on the grid resolution (see Tab. 1 and green circle symbols in Fig. 13). It is larger for coarse grids, the only exception being model #2. Using the MP9 reconstruction scheme, the Maxwell stress converges to a value of $\mathcal{M}_{r\phi} = 0.73 \times 10^{30} \text{ G}^2$ in models #10 and #11 simulated with 67 and 134 grid cells per MRI channel, respectively. The dashed line in Fig. 13 shows that $\mathcal{M}_{r\phi}$ follows roughly a power law with index $-1/3$ as a function of the number of zones per MRI channel, except for the under-resolved model #2 with only eight zones per channel, in which MRI growth terminates at a much smaller value of $\mathcal{M}_{r\phi}$.

This behaviour of $\mathcal{M}_{r\phi}$ can be explained within the parasite model. The KH modes responsible for MRI termination grow from the shear layers created by the MRI channels. During their growth, these secondary instabilities develop structures that are even smaller than the MRI channels. Therefore, to resolve these structures a finer grid is necessary than for the MRI channels themselves. As a result, simulations may not be converged even if the numerically obtained MRI growth rate is close to the theoretical value. Because badly resolved KH modes grow at a rate below the theoretical expectation, parasitic instabilities reach the necessary amplitude to disrupt the channels slightly later during the evolution, and the MRI will terminate at a somewhat higher amplitude than in well-resolved simulations.

The appearance of the outlier (model #2) in Fig. 13 is not surprising. We have already seen that MRI channels are underresolved in this model. Therefore, one would not expect to find any reasonable termination amplitude for this model, i.e. it is probably a chance coincidence that this model gives roughly the same results as the other better resolved models.

For completeness, we included also models #12–#18 in Fig. 13 (red diamond symbols), for which the parasitic modes are restricted not only by the grid resolution but also by the box size and some physical viscosity. The data of these models lie all above the dashed line indicating the influence of resolution alone. Finally, the asterisk symbol marks the result of the ideal MHD model #1, which we discuss in the next subsection.

4.2.5 Influence of viscosity and resistivity

4.2.5.1 Viscosity We have performed the reference simulation (model #7; see Tab. 1), and the set of models described above without any explicit physical viscosity. To study whether a finite physical viscosity corresponding to $Re \approx 100$ (for which the equations of ideal hydrodynamics should still approximately hold) leads to more than mere quantitative changes, we compare the results of models #9 and #12. As expected, in both of these two models, which differ only in the value of the hydrodynamic Reynolds number ($Re = \infty$ for model #9, and $Re \approx 100$ for model #12) the growth of the MRI is terminated by KH modes.

Even though no physical viscosity was used for model #9, it is affected by a non-zero numerical viscosity. To infer the quantita-

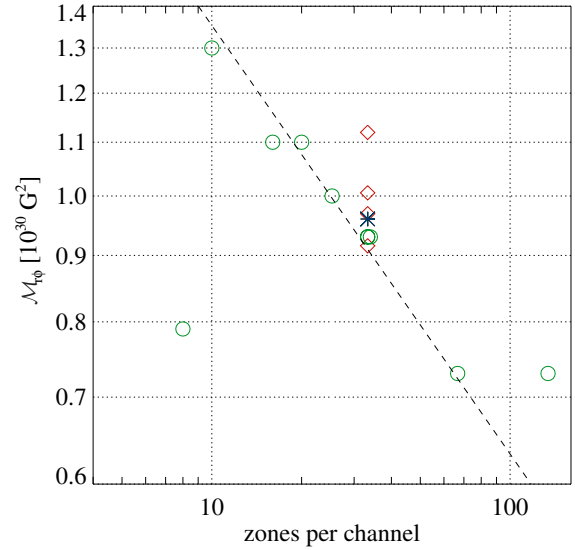


Figure 13. MRI termination amplitudes as a function of grid resolution for models #1 (blue asterisk), #2–#11 (green circles), and #12–#18 (red diamonds), respectively. The dashed line represents a power law in the grid resolution with an index of $-1/3$.

tive importance of the numerical viscosity, we first compare models which differ only in grid resolution in the inviscid limit, e.g., model #9, where the evolution is still notably affected by numerical viscosity, and models #10 and #11, which are already converged, as we have argued in the previous section. We note that the numerical viscosity accounts for the $\approx 22\%$ difference in the volume-averaged Maxwell stress at termination (i.e. the parasitic instabilities are somewhat under-resolved), and has a negligible impact on the MRI growth rate.

We now turn to the comparison of an inviscid model (#9) with one where a physical viscosity has been included (#12). Quantifying the exact contribution of the numerical viscosity in a model that includes also physical viscosity is much more involved. The reasons for this difficulty are multiple. On the one hand, the numerical viscosity is a scale dependent effect, affecting more the smallest scales. Hence, it is relatively more important for the development of parasitic modes than for the MRI growth. On the other hand, the volume-averaged Maxwell stress at termination depends chiefly on a delicate balance between two competing factors. First, models computed with a finite physical viscosity have a smaller γ_{MRI} . Thus, for a similar growth time, $\mathcal{M}_{r\phi}$ should be smaller than for models computed without a physical viscosity. Secondly, this effect is offset, however, by the also smaller growth rate of the KH parasitic modes, which defers the saturation process and allows for a further growth of $\mathcal{M}_{r\phi}$. Thereby, our comparison is of qualitative nature only. In view of the former reasoning, we tentatively attribute the $\sim 4\%$ difference in $\mathcal{M}_{r\phi}$ between the inviscid model #9 and the viscous model #12 to the effect of a finite viscosity in the latter one, though we cannot unambiguously say which part of this difference is caused by numerical viscosity. To support the argument that a finite physical viscosity and not a numerical viscosity is driving the dynamics, we note that the MRI growth rate decreases significantly

in model #12 (as also in all other viscous models from #13 to #18). This expected behaviour (see Section 2.2) implies that including a physical viscosity causes measurable differences already in the MRI growth phase.

4.2.5.2 Resistivity In a final set of simulations, we investigated the influence of a finite (physical) resistivity on MRI termination. Model #1, simulated in ideal MHD, represents the typical conditions prevailing in core collapse supernovae close to the surface of PNS, whereas in models #19 and #20 we explored the (opposite) limit of a very high resistivity. With the latter simulations we also address a prediction of Pessah (2010), namely that for $R_m < 1$, the MRI should be terminated by TM. We performed the ideal MHD simulation of model #1 in the default size box, the results being very similar to those obtained for model #7, which we simulated with the identical setup, but with $R_m \approx 100$.

As expected, the MRI grew in the ideal MHD simulations at a somewhat higher rate ($\gamma_{\text{MRI}} = 1137 \text{ s}^{-1}$), because its growth was not damped by resistivity. We found that the MRI is terminated by parasitic KH instabilities in this model, too. The parasites develop at an angle $\phi_p \approx 45^\circ$ in accordance with the parasite model of GX94. The Maxwell stress at MRI termination is $\mathcal{M}_{r\phi} = 0.96 \times 10^{30} \text{ G}^2$, a value which is similar to those obtained for models #7 and #12 (the latter one being simulated with $R_e \approx R_m = 100$). From these findings we conclude that for Reynolds numbers $R_e, R_m \gtrsim 100$ viscosity and resistivity have no strong influence on the process of MRI termination and the saturation value of the Maxwell stress. However, one should not forget that in all three simulations (i.e. models #1, #19, and #20), numerical resistivity and numerical viscosity do contribute to the 'total' hydrodynamic and magnetic Reynolds numbers (by lowering them).

In the limit of very high resistivity, i.e. for $R_m \ll 1$, the MRI modes that grow fastest in ideal MHD are completely suppressed by magnetic dissipation (PC08). Only modes with sufficiently long wavelengths survive the interplay between MRI amplification and resistive damping in this limiting case, because magnetic dissipation is weaker for these modes. The wavelength of the fastest-growing mode is $\lambda_{\text{MRI}} \propto b_{0z} R_m^{-1}$ (PC08). To keep $\lambda_{\text{MRI}} \approx 0.333 \text{ km}$ in models #19 ($R_m = 0.1$) and #20 ($R_m = 0.05$), we had to reduce the initial magnetic field strength to values of $b_{0z} = 3.25 \times 10^{12} \text{ G}$ and $b_{0z} = 1.63 \times 10^{12} \text{ G}$, respectively.

We find that the fastest MRI mode grows at a considerably slower rate than in the ideal MHD limit in both models, the measured growth rates being $\gamma_{\text{MRI}} = 80 \text{ s}^{-1}$ (model #19) and $\gamma_{\text{MRI}} = 34 \text{ s}^{-1}$ (model #20). These values agree very well with those of PC08, who predicted $\gamma_{\text{MRI}} = 79 \text{ s}^{-1}$ and $\gamma_{\text{MRI}} = 40 \text{ s}^{-1}$, respectively. PC08 also predicted that for $R_e \gg 1$ and $R_m = 0.1$, we should find $\phi_v = 2^\circ$ and $\phi_b = 94^\circ$, i.e. the velocity channels and the magnetic field channels should almost be aligned with the r axis and the ϕ axis, respectively. Indeed, our simulations show that $|b_\phi| \gg |b_r|$, i.e. $\phi_b \approx 90^\circ$, during the exponential growth phase (see Fig. 14).

Finally, according to Pessah (2010), the MRI should be terminated by TM and not KH instabilities for $R_m < 1$. For $R_m = 0.1$, the dominant parasitic mode should have a wavelength

$$\lambda_p = \lambda_{\text{TM}} = 2.1 \lambda_{\text{MRI}} \quad (61)$$

developing at an angle $\phi_p = \phi_b = 94^\circ$. A Fourier analysis of the MRI modes and their parasites (see Fig. 14) shows that shortly before MRI termination ($t \approx 160 \text{ ms}$) the energy stored in horizontal Fourier modes increases significantly growing super-exponentially with time. However, because of numerical noise introduced by our imperfect boundary conditions, we could neither identify parasitic

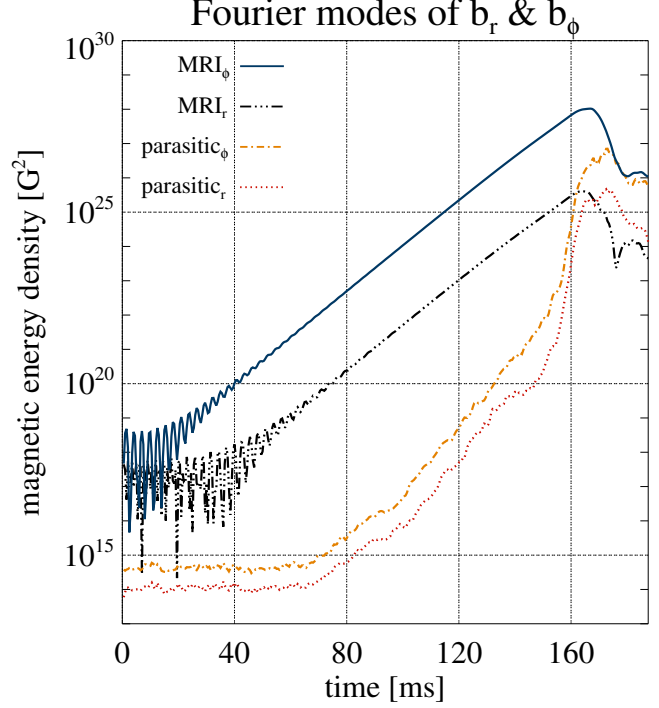


Figure 14. Same as Fig. 11 but for model #19 simulated with a high resistivity ($R_m = 0.1$). Note the very different time-scale at which the MRI evolves in this case.

instabilities nor determine their angle with the help of the Fourier analysis. Therefore, the type of the parasitic instability terminating the MRI in model #19 (as well as in model #20) remains unknown. It is probably neither KH nor TM, because we could not recognise the characteristic features of none of these parasites. The bottom line is that based on models #19 and #20, we cannot confirm the predictions of Pessah (2010) that for $R_m < 1$ the MRI is terminated by TM. As the highly resistive limit is of no direct relevance for core collapse supernovae, we did not investigate this regime in more detail.

5 SUMMARY AND DISCUSSION

Akiyama et al. (2003) first pointed out that the MRI can develop in CCSNe and could lead to a strong amplification of the magnetic field during the proto-neutron star phase. The presence of a dynamically relevant magnetic field is of great interest because it may have implications for the supernova explosion mechanism and for explaining the origin of neutron stars magnetic fields. However, for the typical magnetic field strength present in supernova progenitors, it is necessary to resolve numerically MRI channels with a length scale $\sim 1 \text{ m}$, which makes global simulations unfeasible even with present day supercomputers. To overcome the limitation of global simulations Obergaulinger et al. (2009) performed semi-global simulations in a kilometre size box located near the surface of the proto-neutron star. They confirmed the hypothesis of Akiyama et al. (2003) showing that the MRI can strongly amplify the magnetic field and parasitic instabilities are able to destroy the MRI channels, thereby quenching the amplification of the magnetic field. However, they were unable to identify the agent terminating the MRI growth. Hence, Obergaulinger et al. (2009) could not give an upper limit on the MRI-driven magnetic field amplification.

This work tries to shed some light on the termination process. We numerically studied the evolution of the MRI in the context of a CCSN. To this end, we performed a set of local 3D resistive-viscous MHD simulations in a box representing typical conditions in a proto-neutron star. In all of our simulations we observed the growth of the MRI and its subsequent termination. We identified that secondary KH instabilities are responsible for MRI termination by acting as parasites on the MRI channels. Our results are consistent with the predictions of the parasite model proposed by GX94 and further developed by Latter et al. (2009) and Pessah (2010). Hence, the parasite model, which is based on a local stability analysis of the system, allows some insight into the termination process and provides a valuable guidance for interpreting numerical results. This conclusion was obtained by an analysis of our numerical simulations based on MRI theory and the parasite model in a number of tests:

(i) We observe an exponential growth of MRI channels of a size compatible with the predicted value, λ_{MRI} , for the fastest-growing mode (BH91). The growth rates measured in the numerical simulations agree with those obtained from the local analysis within the simulation box. The presence of viscosity or resistivity lowers the values of the growth rates as expected from theory. In the limit of large hydrodynamic and magnetic Reynolds numbers, $R_e, R_m \gg 1$, the angle between velocity (magnetic field) in the MRI channels and the radial direction is close to the theoretically expected one in the ideal MHD limit by GX94, i.e. $\phi_v = 45^\circ$ ($\phi_b = 135^\circ$).

(ii) For simulations with large hydrodynamic and magnetic Reynolds numbers, $R_e, R_m \gg 1$, the MRI is terminated by KH instabilities, as predicted by GX94 and Pessah (2010) for this regime. To identify the KH instabilities we had to reduce the time interval between outputs of our simulations around termination to a value below the typical growth time of the parasites, in our case 0.1 ms. This explains why Obergaulinger et al. (2009) did not observe the development of KH instabilities, since they employed insufficiently frequent output. To help the analysis we project the magnetic field components into the directions ϕ_v and ϕ_b . Shortly before termination we observe the development of vortex rolls at the position of the shear layer located along an angle $\phi_v = 45^\circ$. We identify the vortices as a consequence of KH instabilities, which eventually disrupt the channels causing turbulence. This behaviour is in agreement with the predictions of GX94 and Pessah (2010).

(iii) Analysing the numerical simulations by means of Fourier transforms, we have been able to determine the properties of the parasitic instabilities, i.e. their horizontal wavelengths and the angles at which they develop. Our results confirm the theoretical predictions of GX94 and Pessah (2010) that for $R_e, R_m \gg 1$ the dominant parasitic instabilities are KH modes developing parallel to the MRI velocity channels (i.e. at an angle $\phi_p \approx 45^\circ$ in the (r, ϕ) plane). The horizontal length of these KH modes is in a reasonable agreement (within a factor of 2) with the predictions of Pessah (2010).

(iv) Motivated by the good agreement with the parasite model, we explored the regime of very high resistivity (i.e. $R_m < 1$), although it is not of direct relevance for CCSNe. In this regime Pessah (2010) predicts that the MRI should be terminated by TMs. To this end we performed two simulations with $R_m = 0.1$ and 0.05, but we were unable to identify the agent terminating the MRI growth, because no clear signature of TM or KH instability could be identified in our simulations. We conclude that possibly even higher resistivities are required for TM to become the dominant secondary instability. A possible explanation of this discrepancy between theory and our simulations is the fact that the calculations of Pessah

(2010) are based on somewhat simplified assumptions. Therefore, his results should be treated more like a guideline rather than exact predictions.

To confirm the above conclusions, we have studied systematically the effect of resistivity, viscosity, box size, and grid resolution. There are a number of numerical artefacts that can affect the simulations:

(i) In axisymmetric (2D) simulations, the MRI growth is terminated by TM. This was already reported by Obergaulinger et al. (2009), who observed TM in their 2D ideal MHD simulations, in accordance with theoretical results obtained by Pessah (2010). Obergaulinger et al. (2009) argued that this resistive MHD instability must have been triggered by numerical resistivity. In 2D simulations only axisymmetric parasitic modes can develop. As axisymmetric KH modes are strongly suppressed by the magnetic field tension of the MRI channels, TM become the dominant secondary instability. They suffer less strongly from this constraint, develop faster than axisymmetric KH modes (but slower than KH modes would grow in full 3D), and terminate the MRI growth. As a result the MRI in 2D is terminated at unrealistically large magnetic stresses and continues to grow after termination, a behaviour not observed in our 3D simulations.

(ii) We performed a set of simulations to study the dependence of the properties of the parasite modes. Using a 9th-order spatial reconstruction scheme (MP9), we reached convergent results only in simulations with at least 60 zones per MRI channel, i.e. the value of the magnetic stress at termination differed by less than 10% between the two highest resolution runs. This grid resolution is significantly higher than the one necessary to obtain convergence in the growth rate of the MRI, for which 8 zones are sufficient to obtain a 10% accuracy. We note that the required number of zones will be significantly higher, if lower order reconstruction methods are used. Our result is not surprising when viewed in the light of the parasite model. The KH instability is triggered by the shear layer between MRI channels. At this layer structures develop that are much finer than the width of the channel itself. Failing to capture the KH instabilities properly because of a lack of resolution leads to artificially large magnetic stresses at MRI termination. However, the qualitative behaviour of the flow seems not to be affected by a lack of resolution. Even for our lowest resolution simulation (8 zones per channel) we are able to identify KH instabilities developing at $\phi_p \approx 45^\circ$ as the main termination agent.

(iii) We studied how the box size can affect the development of parasitic instabilities. In 3D simulations with an azimuthal box length of at least $\approx 1\lambda_{\text{MRI}}$ the MRI is terminated by KH modes, whereas simulations with an azimuthal box length $\lesssim 1\lambda_{\text{MRI}}$ gave very similar results as 2D simulations and the MRI was terminated by TM (because KH modes are suppressed; compare models #16 and #17 in Tab. 1). Taking into account that the parasitic KH instabilities develop at a 45° angle, one should use a box size of at least $1 \approx \lambda_{\text{MRI}}$ in the radial direction. However, we recommend using larger boxes in the horizontal directions to reduce the influence of the boundary conditions on the development of the parasitic instabilities. In the vertical direction it is sufficient to use a box size of λ_{MRI} , i.e. it is sufficient to consider the evolution of one single MRI channel to capture the termination process correctly. Determining the minimum box size has been critical to be able to perform the simulations with the highest resolution presented in this work (model #11 with 134 zones per channel).

Our results have some important implications for the commu-

nity modelling magnetorotational collapse of stellar cores. Studying the termination of the exponential growth phase of the MRI, we learned that it involves parasitic KH instabilities, but does neither depend on the physical resistivity nor viscosity present in CCSNe. The effects of the interaction of neutrinos and matter, which at different locations in the PNS can be described either as an effective viscosity or by a drag term, affect the properties of the MRI, in particular its growth rate and wavelength (Guilet et al. 2015). Consequently, this interaction should induce modifications of the termination amplitude. On the other hand, we do not expect these effects to change the most important qualitative result of our study, namely that the MRI is not terminated by TM, but by the KH instability.

The presence of background flows in CCSNe (like convection or turbulence) can affect the growth and termination of the MRI, too. In 2D global simulations, Cerdá-Durán et al. (2008) observed the growth of coherent channel flows, albeit deformed, while Sawai et al. (2013) observed the disruption of channel flows on timescales of milliseconds due to the presence of a dynamical background. Both, the parasitic instabilities and the effect of the background flow, seem to disrupt channel flows on similar timescales. Therefore, it is likely that both effects will be of relevance in studying the MRI termination in global simulations.

Furthermore, the presence of parasitic instabilities implies the existence of a maximum magnetic stress at termination. This limits the ability of the MRI to amplify the magnetic field to dynamically relevant values in CCSNe. The turbulence triggered by the MRI may amplify the global magnetic field further, if conditions for dynamo action are encountered. A study of the latter process is beyond the scope of this work, and will be addressed in a future publication. The MRI has been traditionally invoked in the CCSN community as a justification to use supernova progenitors with an artificially enhanced initial magnetic field strength, 10^3 – 10^4 times larger than the values expected in stellar evolution models. This argumentation should be revisited if we want to move towards a more realistic modeling of magnetorotational core collapse.

Unfortunately, given the minimum numerical requirements that we provide in this work, 3D simulations seem nowadays unfeasible. To resolve MRI channels of 1 m length scale in a proto-neutron star of about 30 km radius, with a resolution of ~ 60 zones per channel, it would require about 5×10^{19} grid zones. Evolving this system for a typical dynamical timescale of the proto-neutron star evolution, ~ 100 ms, would require about 10^8 time steps, several zettabytes of memory and would consume $\sim 10^{14}$ CPU hours (10^8 iterations times 5×10^{19} zones times 100 operations/zone at 500 Gflops). With current petascale supercomputers this would amount to $\sim 3 \times 10^5$ yr of uninterrupted computation with 100 000 cores. A simulation which includes the whole iron core with a radius of ~ 1000 km would be even more demanding. Reducing the dimensionality of the system by imposing axisymmetry reduces the computational time by a factor $\sim 4 \times 10^6$. The use of adaptive mesh refinement (AMR) techniques would alleviate, but not solve the problem.

The CCSN community has been performing 2D and 3D simulations with resolutions of up to 12.5 m (2D; Sawai et al. 2013) and 15.6 m (3D; Masada et al. 2015). We note that these authors could afford such high resolutions only by accepting other limitations in terms of geometry and input physics, while other simulations use resolutions of several 100 m (Obergaullinger et al. 2006a,b; Shibata et al. 2006; Burrows et al. 2007; Cerdá-Durán et al. 2008; Scheidegger et al. 2008; Mikami et al. 2008; Kuroda & Umeda 2010; Takiwaki & Kotake 2011; Winteler et al. 2012; Mösta et al. 2014; Obergaullinger et al. 2014), which even for the artificially enhanced

initial magnetic field, fail to resolve the termination process of the MRI. Given the above computational requirements, the community should rethink the way to model this scenario. The agreement that we have found here between local simulations and the parasitic instability analysis of GX94 and Pessah (2010) make us hope that there could be a way out. If we can understand how MRI and turbulence work at sub-meter scales, this information could be incorporated in global simulations using appropriate subgrid models. As a first step along this path we plan to gain a deeper understanding in the maximum magnetic stress achievable by the MRI and in the properties of its turbulent saturated state.

ACKNOWLEDGEMENTS

TR acknowledges support from The International Max Planck Research School on Astrophysics at the Ludwig Maximilians University Munich, EM & TR acknowledge support from the Max-Planck-Princeton Center for Plasma Physics, and MA, PCD, TR and MO acknowledge support from the European Research Council (grant CAMAP-259276). We also acknowledge support from grants AYA2013-40979-P and PROMETEOII/2014-069. The authors thank Rob Yates for proof reading the manuscript, and M. Pessah, C. McNally, and H. Latter and J. Guilet for helpful discussions. The authors thank the anonymous referee whose useful remarks greatly improved the quality of this manuscript. The computations have been performed at the Leibniz Supercomputing Center of the Bavarian Academy of Sciences and Humanities (LRZ), the Rechenzentrum Garching of the Max-Planck-Gesellschaft (RZG), and at the Servei d'Informàtica of the University of Valencia.

REFERENCES

- Akiyama, S., Wheeler, J. C., Meier, D. L., & Lichtenstadt, I. 2003, *ApJ*, 584, 954
- Balbus, S. A. 1995, *ApJ*, 453, 380
- Balbus, S. A. & Hawley, J. F. 1991, *ApJ*, 376, 214
- Balbus, S. A. & Hawley, J. F. 1998, *Reviews of Modern Physics*, 70, 1
- Bodo, G., Mignone, A., Cattaneo, F., Rossi, P., & Ferrari, A. 2008, *A&A*, 487, 1
- Brandenburg, A. 2005, *Astronomische Nachrichten*, 326, 787
- Burrows, A., Dessart, L., Livne, E., Ott, C. D., & Murphy, J. 2007, *ApJ*, 664, 416
- Cerdá-Durán, P., Font, J. A., & Dimmelmeier, H. 2007, *A&A*, 474, 169
- Cerdá-Durán, P., Font, J. A., Antón, L., Müller, E. 2008, *A&A*, 492, 937
- Chandrasekhar, S. 1960, *Proceedings of the National Academy of Science*, 46, 253
- Evans, C. R. & Hawley, J. F. 1988, *ApJ*, 332, 659
- Fromang, S. & Papaloizou, J. 2007, *A&A*, 476, 1113
- Fromang, S., Papaloizou, J., Lesur, G., & Heinemann, T. 2007, *A&A*, 476, 1123
- Gardiner, T. A. & Stone, J. M. 2005, in *American Institute of Physics Conference Series*, Vol. 784, *Magnetic Fields in the Universe: From Laboratory and Stars to Primordial Structures*, ed. E. M. de Gouveia dal Pino, G. Lugones, & A. Lazarian, 475–488
- Goodman, J. & Xu, G. 1994, *ApJ*, 432, 213
- Guilet, J., Müller, E. & Janka, H. T. 2015, *ApJ*, 447, 3992

- Guilet, J. & Müller, E. 2015, MNRAS, 450, 2153
- Harten, A. 1983, J. Comput. Phys., 49, 357
- Hawley, J. F. & Balbus, S. A. 1991, ApJ, 376, 223
- Balbus, S. A. & Hawley, J. F. 1992, ApJ, 400, 595
- Heger, A., Woosley, S. E., & Spruit, H. C. 2005, ApJ, 626, 350
- Keil, W., Janka, H.-T., & Müller, E. 1996, ApJL, 473, L111+
- Klahr, H. H. & Bodenheimer, P. 2003, ApJ, 582, 869
- Knobloch, E. & Julien, K. 2005, PhFl, 17, 094106
- Kuroda, T., & Umeda, H. 2010, ApJS, 191, 439
- Latter, H. N., Lesaffre, P., & Balbus, S. A. 2009, MNRAS, 394, 715
- Lesaffre, P., Balbus, S. A., & Latter, H. 2009, MNRAS, 396, 779
- LeVeque, R. J. 1992, Numerical Methods for Conservation Laws, 2nd edn., Lectures in mathematics - ETH Zürich (Birkhäuser)
- Levy, D., Puppo, G., & Russo, G. 2002, SIAM J. Sci. Comput., 24, 480
- Masada, Y., Sano, T., & Shibata, K. 2007, ApJ, 655, 447
- Masada, Y., Takiwaki, T., Kotake, K., & Sano, T. 2012, ApJ, 759, 110
- Masada, Y., Takiwaki, T., & Kotake, K. 2015, ApJL, 798, L22
- Meier, D. L., Epstein, R. I., Arnett, W. D., & Schramm, D. N. 1976, ApJ, 204, 869
- Menou, K., Balbus, S. A., & Spruit, H. C. 2004, ApJ, 607, 564
- Mikami, H., Sato, Y., Matsumoto, T., & Hanawa, T. 2008, ApJ, 683, 357
- Miyoshi, T., & Kusano, K. 2005, Journal of Computational Physics, 208, 315
- Mösta, P., Richers, S., Ott, C. D., et al. 2014, ApJL, 785, L29
- Obergaulinger, M. 2008, PhD thesis, Technische Universität München
- Obergaulinger, M., Cerdá-Durán, P., Müller, E., & Aloy, M. A. 2009, A&A, 498, 241
- Obergaulinger, M., Aloy, M. A., & Müller, E. 2006b, A&A, 450, 1107
- Obergaulinger, M., Aloy, M. A., Dimmelmeier, H., & Müller, E. 2006a, A&A, 457, 209
- Obergaulinger, M., Janka, H.-T., & Aloy, M. A. 2014, MNRAS, 445, 3169
- Pessah, M. E., & Chan, C.-k. 2008, ApJ, 684, 498
- Pessah, M. E., & Goodman, J. 2009, ApJL, 698, L72
- Pessah, M. E. 2010, ApJ, 716, 1012
- Rembiasz, T. 2013, PhD thesis, Technische Universität München.
<https://mediatum.ub.tum.de/doc/1183388>
- Sano, T. & Inutsuka, S.-i. 2001, ApJL, 561, L179
- Sano, T., Inutsuka, S.-i., Turner, N. J., & Stone, J. M. 2004, ApJ, 605, 321
- Sawai, H., Yamada, S., & Suzuki, H. 2013, ApJL, 770, L19
- Sawai, H., & Yamada, S. 2015, arXiv:1504.03035
- Scheidegger, S., Fischer, T., Whitehouse, S. C., & Liebendörfer, M. 2008, A&A, 490, 231
- Shakura, N. I. & Sunyaev, R. A. 1973, A&A, 24, 337
- Shibata, M., Liu, Y. T., Shapiro, S. L., & Stephens, B. C. 2006, Phys. Rev. D, 74, 104026
- Suresh, A. & Huynh, H. 1997, J. Comput. Phys., 136, 83
- Takiwaki, T., & Kotake, K. 2011, ApJ, 743, 30
- Thompson, C. & Duncan, R. C. 1993, ApJ, 408, 194
- Toro, E. F. & Titarev, V. A. 2006, J. Comput. Phys., 216, 403
- Velikhov, E. 1959, Sov. Phys. JETP, 36, 995
- Winteler, C., Käppeli, R., Perego, A., Arcones, A., Vassetz, N., Nishimura, N., Liebendörfer, M., Thielemann, F.-K., 2012, ApJL, 750, L22